

# 1 **Trabecular bone remodeling in the ageing mouse: a micro-multiphysics** 2 **agent-based *in silico* model using cell-type-specific mechanomic profiles**

3 **Daniele Boaretti<sup>1</sup>, Francisco C. Marques<sup>1</sup>, Charles Ledoux<sup>1</sup>, Amit Singh<sup>1</sup>, Jack J. Kendall<sup>1</sup>,**  
4 **Esther Wehrle<sup>1,2</sup>, Gisela A. Kuhn<sup>1</sup>, Yogesh D. Bansod<sup>1</sup>, Friederike A. Schulte<sup>1</sup>, Ralph Müller\*<sup>1</sup>**

5 <sup>1</sup>Institute for Biomechanics, ETH Zurich, Zurich, Switzerland

6 <sup>2</sup>AO Research Institute Davos, Davos Platz, Switzerland

7

8 **\* Correspondence:**

9 Ralph Müller  
10 ram@ethz.ch

11 **Keywords: Single-cell mechanotransduction, bone remodeling, bone adaptation, micro-**  
12 **multiphysics agent-based modeling, *in silico*.**

## 13 **Abstract**

14 Bone remodeling is regulated by the interaction between different cells and tissues across many  
15 spatial and temporal scales. *In silico* models have been of help to further understand the signaling  
16 pathways that regulate the spatial cellular interplay. We have established a 3D multiscale micro-  
17 multiphysics agent-based (micro-MPA) *in silico* model of trabecular bone remodeling using  
18 longitudinal *in vivo* data from the sixth caudal vertebra (CV6) of PolgA<sup>(D257A/D257A)</sup> mice, a mouse  
19 model of premature aging. Our model includes a variety of cells as single agents and receptor-ligand  
20 kinetics, mechanotransduction, diffusion and decay of cytokines which regulate the cells' behavior.  
21 The micro-MPA model was applied for simulating trabecular bone remodeling in the CV6 of 5 mice  
22 over 4 weeks and we evaluated the static and dynamic morphometry of the trabecular bone  
23 microarchitecture. We identified a configuration of the model parameters to simulate a homeostatic  
24 trabecular bone remodeling. Additionally, our simulations showed different anabolic, anti-anabolic,  
25 catabolic and anticatabolic responses with an increase or decrease by one standard deviation in the  
26 levels of osteoprotegerin (OPG), receptor activator of nuclear factor kB ligand (RANKL), and  
27 sclerostin (Scl) produced by the osteocytes. From these results, we concluded that OPG inhibits  
28 osteoclastic bone resorption by reducing the osteoclast recruitment, RANKL promotes bone  
29 resorption by enhancing the osteoclast recruitment and Scl blocks bone formation by inhibiting  
30 osteoblast differentiation. The variations in trabecular bone volume fraction and thickness (BV/TV  
31 and Tb.Th) were relatively higher with variations of one standard deviation in the levels of RANKL  
32 compared to OPG and Scl. This micro-MPA model will help us to better understand how cells  
33 respond to the mechanical signal by changing their activity in response to their local mechanical  
34 environment.

## 35 **Introduction**

36 With aging, bone becomes more fragile with increasing fracture risk, leading to an increased  
37 morbidity and mortality and to an economic burden of € 57 billion in 2019 in the European Union  
38 plus Switzerland and the United Kingdom (Kanis et al. 2021). To better understand how aging affects

39 bone cellular behavior, *in vivo* and *in silico* studies have been used to analyze the tissue and cellular  
40 properties of bone mechanobiology. It is known that bone remodeling is regulated by the interaction  
41 between different cells and tissues across many spatial and temporal scales. Yet, bone remodeling has  
42 not been quantitatively studied *in silico* across spatial and temporal scales and using 3D *in vivo* data  
43 as reference. Hybrid modeling has been identified as a powerful modeling technique which combines  
44 multiscale, multiphysics, and agent-based modeling to analyze in a unified way the organ, tissue, cell,  
45 and gene scales over weeks, months or even years (Boaretti et al. 2022). Such an *in silico* model can  
46 deal with the action of single cells while millions of cells are active and interact with each other in a  
47 multiscale simulation, making this tool ideal to explore the hierarchical processes governing bone  
48 mechanobiology. Furthermore, by enabling fine modelling of signaling pathways that regulate the  
49 cell's activity, such models can help to estimate physiological cytokine production rates and explore  
50 their effect on spatial cellular distribution, bone formation, and bone resorption, which is hardly  
51 feasible *in vivo*.

52 Recent experimental studies have analyzed the effects of aging in mice and how loading can  
53 counterbalance frailty (Scheuren et al. 2020a, b). Accelerated aging was provoked in  
54 PolgA<sup>(D257A/D257A)</sup> mice due to systemic mitochondrial dysfunction caused by accumulation of  
55 mitochondrial DNA point mutations (Trifunovic et al. 2004; Kujoth et al. 2005). The findings from  
56 these works have mainly focused on cortical and trabecular bone morphometric parameters with  
57 analyses of selected gene and protein expression on specific time points. The work of Dobson and  
58 colleagues (Dobson et al. 2020) showed that in this PolgA<sup>(D257A/D257A)</sup> mouse model, osteoblast  
59 density was reduced and the production of mineralized matrix by osteoblasts was significantly  
60 impaired, leading to reduced bone formation rates. The mechanisms which lead to cellular alterations  
61 in bone with aging remain to be further elucidated.

62 We have recently proposed an *in silico* multiscale micro-multiphysics agent-based (micro-MPA)  
63 model of fracture healing in cortical bone adapted from the model of Tourolle (Tourolle 2019) and  
64 adapted by Boaretti (Boaretti et al. 2018). This micro-MPA model is based on multiscale (from the  
65 organ to the protein spatial scales and from weeks to minutes as temporal scales), multiphysics  
66 (mechanical signal, reaction-diffusion-decay of cytokines), and agent-based modelling (single-cell  
67 behavior and mechanotransduction). Each cell is modelled as a single agent, and signaling pathways  
68 were modeled to regulate the cell behavior. In this model, osteoprotegerin (OPG), receptor activator  
69 of nuclear factor  $\kappa$ B ligand (RANKL), sclerostin (Scl) are cytokines that decay, diffuse in the  
70 volume, and are produced by the cells. Transforming growth factor beta 1 (TGF- $\beta$ 1) is modelled as  
71 cytokine stored in the bone volume and it can diffuse and decay after resorption. The signaling  
72 pathways were modelled with receptor-ligand kinetics, with the receptors located on the cells'  
73 surfaces. In addition, a free ligand can bind to another free ligand, e.g., OPG can bind to RANKL.  
74 These pathways have been shown to be the main regulators of cell differentiation and proliferation  
75 (Krishnan et al. 2006; Boyce and Xing 2008; Lin et al. 2009; Tang et al. 2009; Warren et al. 2015;  
76 Elson et al. 2022). The osteocytes were considered the main mechanosensors of the mechanical  
77 signal (Santos et al. 2009; Klein-Nulend et al. 2012, 2013) and they promoted bone formation or  
78 resorption by releasing cytokines into the volume to regulate the signaling pathways affecting  
79 eventually the osteoblasts and osteoclasts. These cells form and resorb bone on the surface,  
80 respectively. Osteocytes, osteoblasts and osteoclasts were the basis for the regulation of bone  
81 remodeling we can simulate using *in vivo* data. Indeed, a previous version of this model was used for  
82 simulating denosumab treatment in human biopsies over 10 years, showing the potential of micro-  
83 MPA models for designing optimal clinical trials (Tourolle et al. 2021).

84 In the current study, we used this micro-MPA model to simulate how bone adapts and remodels  
85 through single-cell mechanotransduction in mice. We hypothesized that cells produce cytokines to  
86 regulate the cellular actions as a response to the local mechanical signal they perceive, e.g., cells  
87 release cytokines to promote anabolic or anticatabolic responses under high stress and cells release  
88 catabolic or anti-anabolic cytokines under low stress. Furthermore, we hypothesized that osteocytes  
89 are mainly responsible for regulating the other cells' activity through their single-cell cytokine  
90 production.

91 The aim of this work is to show that the proposed *in silico* model can reproduce a homeostatic  
92 condition similar to the longitudinal *in vivo* data, where a dynamic equilibrium between bone  
93 formation and bone resorption maintains relatively constant bone volume fraction (Rodan 1998;  
94 Nakahama 2010; Rauner et al. 2020). Moreover, we investigated the quantitative effect of  
95 manipulating the cytokines levels involved in the signaling pathways on the bone morphometric  
96 parameters. For this purpose, the proposed novel micro-MPA *in silico* model of bone remodeling was  
97 applied to micro-computed tomography (micro-CT) *in vivo* data to test the effect of different  
98 production values of RANKL, OPG, and Scl by osteocytes on the static and dynamic bone  
99 morphometry data relatively to the homeostatic configuration.

## 100 **Materials and Methods**

### 101 ***In vivo* input data**

102 *In vivo* data of the control group of a study analyzing the effects of frailty and osteosarcopenia on the  
103 bone microarchitecture of prematurely aged PolgA<sup>(D257A/D257A)</sup> mice (n=9) were used (Scheuren et al.  
104 2020a). Briefly, at an age of 35 weeks, stainless steel pins were inserted at the sixth caudal vertebra  
105 (CV6). At week 38, a sham cyclic loading regime was applied three times per week over 4 weeks.  
106 The *in vivo* micro-CT images (vivaCT 40, Scanco Medical AG) were acquired and analyzed every  
107 week at an isotropic voxel resolution of 10.5  $\mu\text{m}$ , see Figure 1A. The acquired images showed a  
108 slight reduction in the normalized trabecular bone volume fraction over the course of the experiment  
109 (2% at the end), see **Error! Reference source not found.****Error! Reference source not found.**

### 110 ***In silico* micro-multiphysics agent-based model**

111 The micro-MPA model was originally developed for simulating fracture healing in the mouse femur  
112 (Tourolle 2019). In the present work, we adapted this micro-MPA model for the simulation of  
113 homeostatic bone remodeling in the mouse vertebra, including the bone response to physiological  
114 loading. The overview of the adapted *in silico* model is shown in Figure 2.

115 In the current implementation, the cells are modeled individually using the agent-based paradigm,  
116 where all cells of the same type share the same biological properties and follow the same prescribed  
117 rules. The model implements the actions of each cell according to the local physiological, chemical,  
118 and mechanical environment at the cellular spatial and temporal scale. In our implementation, the  
119 changes in the bone microarchitecture are accumulated over the whole time of the experiment (4  
120 weeks) which is much longer than the single temporal step of the cells (40 minutes). The model  
121 simulated bone remodeling only within the trabecular region, while the cortical region was kept  
122 constant during the simulation. This approach was used also in other works by Schulte and Levchuk  
123 (Schulte et al. 2013; Levchuk et al. 2014; Levchuk 2015).

## 124 **Modeling the cellular behavior**

125 Osteocytes (Ot) are embedded in bone and produce RANKL, OPG, and Scl depending on the local  
126 mechanical signal they perceive (Santos et al. 2009; Klein-Nulend et al. 2012, 2013). Osteoblasts  
127 (Ob) produce osteoid, unmineralized matrix, in their neighborhood towards the surface of the bone,  
128 based on the local effective strain they perceive. Moreover, Ob may become pre-Ot when the voxel  
129 they reside in is at least 50% full of osteoid and there is an osteocyte in the normal direction towards  
130 the bone (Franz-Odenaal et al. 2006). Lining cells are considered osteoblasts precursors. In addition,  
131 Ob and lining cells also produce OPG and RANKL accordingly to the mechanical signal they  
132 perceive. Mesenchymal stem cells (MSC) are present in the marrow space where they can move,  
133 proliferate, undergo apoptosis, and can differentiate into an Ob or a lining cell if they are close to the  
134 surface and close to an Oc. MSC, lining cells, and Ob have the Lipoprotein receptor-related protein  
135 5/6 (LRP5/6) receptor which binds to Scl (Li et al. 2005; Bourhis et al. 2011). If the bound receptor is  
136 higher than a user-defined threshold value, Ob differentiate into lining cell and MSC differentiate  
137 into lining cell if they meet the condition mentioned above. MSC and Ob have also the TGF- $\beta$ 1  
138 receptor on their surface, and if that receptor is highly bound then they can proliferate more  
139 frequently. Pre-Ot differentiate into Ot if the voxel they reside in is at least 50% full of mineralized  
140 matrix (Franz-Odenaal et al. 2006). The hematopoietic stem cells (HSC) are present in the marrow  
141 space, they can move, proliferate, undergo apoptosis and differentiate into pre-Oc if their RANK  
142 receptors are highly bound to RANKL (Nelson et al. 2012; Warren et al. 2015). Pre-Oc are motile  
143 and can differentiate back into HSCs if the RANK receptor is not highly bound. Moreover, they can  
144 differentiate into Oc if there are at least 3 osteoclastic cells (pre-Oc or Oc) in their neighborhood. Oc  
145 resorb bone towards the bone surface, with the direction defined by the gradient of the mineral  
146 concentration. We modeled the mineralization of the matrix in each voxel by changing its mineral  
147 concentration to reach its osteoid concentration. Therefore, given a voxel, if there is more osteoid  
148 than mineral, the mineral concentration will increase and if there is more mineral than osteoid, the  
149 mineral concentration will decrease. In this way, when Ob release osteoid, there is a delay in bone  
150 formation because osteoid leads to a change in the mineral concentration through the mineralization  
151 process.

152 To simulate trabecular bone remodeling, we modeled TGF- $\beta$ 1, RANKL-RANK-OPG, and LRP5/6-  
153 Scl signaling pathways at the receptor-ligand level and the Ob, lining cell, Oc, pre-Oc, Ot, pre-Ot,  
154 MSC, HSC at the cellular level.

## 155 **Application of the model to simulate bone remodeling in mouse vertebrae**

156 The overview of the simulation algorithm can be seen in Figure 2B. Each voxel has a value of bone  
157 mineral density from 0 to 1160 mg HA/cm<sup>3</sup> and this value is converted to greyscale values ranging  
158 from 0 to 1 with linear scaling. We considered the grayscale bone density values from 0.5 to 1 as  
159 bone tissue. The minimum value of 0.5 corresponds to a bone density value of 580 mg HA/cm<sup>3</sup>  
160 which is the same threshold value employed previously for the postprocessing of the original  
161 corresponding *in vivo* data (Scheuren et al. 2020a).

162 The mechanical signal was obtained using the micro-finite element (micro-FE) analysis. For this  
163 purpose, the bone tissue and marrow voxels of CV6 vertebrae were converted to Young's modulus  
164 values as performed previously (Webster et al. 2008). The effective strain computed from this  
165 analysis was used as the mechanical signal of the cells (Mullender et al. 1996; Schulte et al. 2013).  
166 This variable was used for the single cell production: each cell produces an amount of cytokines  
167 following a specific mechanotransduction curve, with a sigmoidal shape to represent the anabolic  
168 (OPG) and catabolic (RANKL, Scl) response to the mechanical signal. For each cytokine-cell



169 production, the Hill curve was defined for both marrow and bone cells with a specific maximum  
170 value, hill coefficient and  $mech_{thres}$  which is the value of the mechanical signal corresponding to  
171 half of the maximum value produced by a cell. These values were defined specimen-specific in order  
172 to take into account the variability of the mechanical environment between different animals.

173 The definition of the Hill parameters was calibrated to have a higher production of cytokines in  
174 regions where the local mechanical signal, Gaussian-dilated effective strain ( $\epsilon$ ), is relatively higher or  
175 lower for anabolic, anticatabolic cytokines or catabolic, anti-anabolic cytokines, respectively. The  
176  $mech_{thres}$  for bone cells is defined for every vertebra as follows:

177  $mech_{thres}^{bone} = 0.95 * median(\epsilon|_{bone})$  where  $\epsilon|_{bone}$  is the local mechanical signal in the trabecular  
178 region of the given vertebra. The mechanotransduction for the marrow cells that can release products  
179 into the volume is defined using this mechanostat threshold:

180  $mech_{thres}^{marrow} = 0.45 * median(\epsilon|_{marrow})$  where  $\epsilon|_{marrow}$  is the local mechanical signal in the  
181 trabecular region of the marrow of the given vertebra. In particular,  $\epsilon|_{marrow}$  is the gaussian dilated  
182 effective strain in the trabecular marrow voxels and is used as input of the mechanotransduction  
183 function for the osteoclasts, determining how much bone is resorbed based on the signal.

184 Analogously,  $\epsilon|_{marrow}$  is used as input of the mechanotransduction function for the osteoblasts and  
185 lining cells, determining how much cytokines and osteoid are added to the specific voxel.

186 The model was implemented according to the following multiscale temporal discretization. The  
187 cellular behavior we described in 2.2.1 was simulated with a 40-minute time step ( $dt_{cells-RDD}$ ).  
188 Following the simulations obtained by Tourolle (Tourolle 2019), this value turned out to be  
189 sufficiently similar to the values observed experimentally about motility and activity of the bone  
190 cells. The proteins and other present chemical substances in the *in silico* simulation were simulated to  
191 React, Diffuse, Decay (RDD, Figure 2C) with the same time step for the cells  $dt_{cells-RDD}$ , subdivided  
192 into 10 equal temporal substeps of 4 minutes through Strang splitting (Strang 1968).

193 In comparison to the implementation introduced in the model of reference, a new parallelized  
194 approach has been used where the chemical substances and the cells have been subdivided into  
195 subdomains. The subdivision in subdomains was carried out to minimize the volume of data from  
196 one subdomain to the other. Then, the model computes the spatio-temporal evolution of the cells and  
197 signaling pathways and RDD with the timestep  $dt_{cells-RDD}$  in parallel across the subdomains. The  
198 micro-FE of the vertebra is computed for updating the mechanical signal perceived by the cells with  
199 a predefined update interval of 8 hours ( $dt_{micro-FE}$ ), which is higher than  $dt_{cells-RDD}$  to simulate a delay  
200 in the perception of the new mechanical signal.

## 201 **Model generation**

202 The trabecular region was automatically obtained for each sample as described previously (Lambers  
203 et al. 2011) comprising a lattice of up to 200x200x300 voxels of the same resolution of *in vivo* data,  
204 hence 12 million voxels. In a first step, the greatest connected component (GCC) of the vertebra was  
205 defined. The bone phase of the trabecular region (bone mineral density greater than 580 mg HA/cm<sup>3</sup>),  
206 was then used for setting the initial mineral and osteoid concentrations (1). The marrow of the  
207 trabecular region was seeded with MSCs and HSCs with a density of 1.25 x 10<sup>7</sup> cells/ml. Ob and Oc  
208 were seeded randomly occupying a portion of the bone surface. The binding sites of the cells were  
209 modified to make the multicellular system closer to a real state, where the cells' receptors are  
210 partially or fully bound. Ot were seeded using an exponential distribution to have more osteocytes  
211 embedded deeper in bone rather than close to the bone surface. The seeding of all cells in a cross-  
212 sectional slice can be seen in Figure 2D. The cytokines were defined using experimental data  
213 obtained from the literature, when available, see Supplementary Table S1. Missing concentrations

214 were defined using calibrated values after running simulations and checking whether the cells would  
215 reside and be active in corresponding biochemical regions, e.g. Oc resorb bone and lining cells are  
216 present mainly in low strain regions whereas Ob release osteoid primarily in high strain regions. The  
217 summary of the initial concentrations is defined in Supplementary Table S1.

218 The model started running without changes to the bone microarchitecture for 48 iterations  
219 (corresponds to 2 days), see Figure 2B, to enable a more adequate spatial arrangement of the cells  
220 and cytokines. This pre-processing step is needed because the micro-CT image used as input contains  
221 only information regarding the bone microarchitecture. The final configuration after this initialization  
222 is illustrated in Figure 2E, where for simplicity reasons only the surface cells, the RANK binding site  
223 occupancy for osteoclasts and preosteoclasts and the spatial RANKL distribution in the trabecular  
224 region are shown. The model then continued running with changes to bone microarchitecture for five  
225 days to enter the active bone remodeling phase and to reduce the dependency of the initial data,  
226 where the distributions of the cells, proteins and receptors were affected by uncertainty or absence of  
227 such input data. The result of this phase was considered as the initial state for the homeostatic as well  
228 as for the simulations where the maximum amount of OPG, RANKL and Scl produced by osteocytes  
229 are changed.

### 230 **Design of simulations**

231 In this work, we simulated homeostatic remodeling and we tested the effects of different production  
232 values of RANKL, OPG, and Scl by osteocytes on the static and dynamic bone morphometry data  
233 relatively to the homeostatic remodeling. For each condition different from homeostatic, one  
234 parameter was increased or decreased at the time and the parameters were kept constant. This  
235 approach was used regardless of the simulated animal. Each condition was simulated using *in vivo*  
236 data of 5 CV6 vertebrae. The output of the homeostatic condition was compared against the *in vivo*  
237 data and against the simulated conditions of higher and lower production values of OPG, RANKL  
238 and Scl separately.

239 First, homeostatic remodeling was simulated with a set of 41 parameters that were kept constant  
240 regardless of the simulated animal (Supplementary Table S2). 37 parameters were optimized for a  
241 balanced spatiotemporal evolution of the cytokines, cell differentiation, bone formation and bone  
242 resorption, while other values were set accordingly to literature. They range from the frequency of  
243 random movement of the cells, thresholds regulating the differentiation of the cells, binding site  
244 numbers, osteoblast and osteoclast polarization factors, osteoblast and osteoclast cluster size,  
245 proliferation and apoptosis rates of cells (especially osteoblasts, MSC, HSC), mechanostat  
246 coefficients, the maximum single-cell production rate of cytokines, diffusion and decay coefficients  
247 for the cytokines, mineralization rate. The motility parameters are presented as probability values of  
248 movement of 1 voxel per  $dt_{\text{cells-RDD}}$  in a range of 0 to 1. The Ob and Oc polarization coefficients are  
249 values that represent the tendency of these cells to add osteoid or resorb bone, respectively, towards  
250 the gradient of the mineral concentration from their position (Tourolle 2019). The competitive  
251 reaction RANKL-RANK-OPG requires the definition of the forward and backward binding  
252 coefficients for the RANKL-RANK and RANKL-OPG complexes, whereas the simple receptor-  
253 ligand kinetics LRP5/6-Scl requires the definition of the forward and backward binding coefficients  
254 for the complex LRP5/6-Scl.

255 After the simulations of homeostatic remodeling, we investigated whether OPG inhibits osteoclast  
256 reorption. An increased OPG production was modelled as an anabolic response to higher effective  
257 strains by means of reducing Oc recruitment. With higher or lower OPG levels, OPG binds to  
258 RANKL leading to lower or higher availability of free RANKL that can bind to the RANK receptors

259 on Oc cells, thus leading to lower Oc recruitment. Then, we investigated whether RANKL promotes  
260 bone resorption. RANKL was modelled as a cytokine produced by Ob, Ot and lining cells as a  
261 catabolic response when these cells perceive lower values of effective strains to promote Oc  
262 recruitment and eventually favor bone resorption. Lastly, we investigated whether Scl blocks bone  
263 formation by inhibiting osteoblasts. Scl was modeled as cytokine produced by Ot as an anti-anabolic  
264 response when these cells perceive lower values of effective strains. These three hypotheses were  
265 tested separately by changing the maximum production of OPG, RANKL and Scl by a single Ot,  
266 ( $\beta_{Ot}^{OPG}$ ,  $\beta_{Ot}^{RANKL}$ ,  $\beta_{Ot}^{Scl}$ ) in the simulations using the values reported in Supplementary Table S3,  
267 Supplementary Table S4 and Supplementary Table S5. Starting from the baseline value reported in  
268 Supplementary Table S2, these higher and lower values were obtained by adding or subtracting the  
269 rescaled standard deviation of the serum concentrations levels reported by Shahnazari and colleagues  
270 (Shahnazari et al. 2012).

## 271 **Bone morphometry and visualization**

272 Static morphometric parameters analyzed were bone volume fraction (BV/TV), specific bone surface  
273 (BS/BV), bone surface density (BS/TV), trabecular thickness (Tb.Th), trabecular spacing (Tb.Sp),  
274 and trabecular number (Tb.N). We computed them for each day of the simulation. Dynamic  
275 parameters were mineral apposition rate (MAR), mineral resorption rate (MRR), bone formation rate  
276 (BFR), bone resorption rate (BRR), mineralizing surface (MS), and eroded surface (ES). They were  
277 computed by overlaying the images with a time interval of 2 weeks as analyzed in recent publications  
278 (Scheuren et al. 2020a, b), using the image processing language (XIPL, (Hildebrand et al. 1999)).  
279 Our simulation involved only the trabecular region while the cortical region is unchanged over time,  
280 contrary to the *in vivo* data which show cortical remodeling occurs as well. Static parameters between  
281 different datasets were compared as percent changes by normalizing the values to the initial value of  
282 the morphological parameter of interest while dynamic parameters were compared as absolute values.

283 The trabecular 3D bone microarchitecture was visualized using ParaView (Kitware, Version 5.10;  
284 Clifton Park, NY). The formed, quiescent and resorbed (FQR) regions in the *in vivo* images were  
285 obtained after registration of the acquired images and their overlapping. The FQR regions in the *in*  
286 *silico* images were directly obtained by overlapping the images at different time points.

## 287 **Software and platform used**

288 A hybrid C++/Python code (Python Language Reference, Version 3.8) that expanded from the  
289 original implementation of the model was used to perform the simulations (Tourolle 2019). The  
290 implementation is made available through Python bindings with pybind11 (Jakob et al. 2017). Taking  
291 advantage of the other packages used for image processing, analysis and parallelization, we used  
292 Python as the front-end. In particular, we used the mpi4py package for managing the MPI parallel  
293 distributed computing interface in Python (Dalcin et al. 2011). We employed distributed and shared  
294 parallel computing paradigms (OpenMP and MPI) due to the high number of variables used in the  
295 simulations. We used the MPI parallel version of an algebraic multigrid solver, AMGCL, to solve the  
296 diffusion problem of the cytokines into the volume (Demidov 2019). The Swiss National  
297 Supercomputing Center (CSCS, Lugano, Switzerland) computational platform (STATE SYSTEM)  
298 was used for running the simulations. Each node has 36 cores which can be scheduled to work in a  
299 customized way regarding memory and parallelization of tasks. The parallel solver for the spatio-  
300 temporal step of the cells and cytokines required 8 nodes to have enough memory and sufficient  
301 speedup. For these resources, we use 4 MPI tasks for each node and 9 OMP threads. Additionally, the  
302 micro-FE vertebral models were solved using 2 nodes using ParOsol, a parallel solver designed for  
303 micro-FE analysis based on micro-CT images (Flaig and Arbenz 2011). The number of nodes was

304 chosen in order to have a good trade-off between computational time and speed-up of the code. These  
305 two solvers were combined to obtain a suitable environment for solving the interconnected  
306 mechanical environment and the tissue, cellular and signaling pathways with a resolution of 10.5  $\mu\text{m}$ .

### 307 **Statistical analysis**

308 Statistical analysis was performed in R (R Core Team (2019), R Foundation for Statistical  
309 Computing, Vienna, Austria). The R lmerTEST package (Kuznetsova et al. 2017) was used to  
310 perform the linear mixed model. The linear mixed-effects models account for “intra-correlations”  
311 between the *in silico* simulations and *in vivo* repeated measurements. The model is described in two  
312 parts: fixed effects and random effects. The random effects part accounts for the intra-correlations of  
313 repeated measures in *in vivo* samples and *in silico* simulations or the high/medium/low production  
314 level of OPG, RANKL and Scl. The fixed-effects part accounts for the impact of various covariates  
315 over time on outcomes on an average level of the dynamic and static bone morphometric parameters.  
316 Furthermore, the likelihood ratio test was performed to assess the goodness of fit of three nested  
317 models based on the ratio of their likelihoods. All the nested model equations are in the  
318 supplementary section (Supplementary Material 1.1). The significance level between the groups (*in*  
319 *vivo* data/*in silico* simulation or high/low, high/medium, medium/low) was calculated using pairwise  
320 comparisons with Tukey’s post-hoc correction for multiple comparisons. The significance level for  
321 the interaction between time and group was calculated using ANOVA with the linear-mixed model.  
322 The mean and the standard error of the mean were plotted and p-values smaller than 0.05 were  
323 considered significant (Lenth 2022).

### 324 **Results**

325 To study trabecular bone remodeling, we ran our micro-MPA model on five CV6 vertebrae from  
326 mice obtained using micro-CT imaging. Thanks to the use of high-performance computing, the  
327 computational capability and the efficiency of the computational code were increased, allowing the  
328 simulation of thousands of cells and RDD of proteins in a complete trabecular volume. A simulation  
329 of 4 weeks took usually 3 to 6 hours on a supercomputer. More time was required with a bigger  
330 trabecular volume (TV) or when the finite-element analysis required more iterations for converging  
331 to a numerical solution. A single cell and RDD step took usually up to 10 s, whereas solving a single  
332 micro-FE analysis took less than a minute. First, we report the results of homeostatic remodeling  
333 compared to the *in vivo* data. Then, to demonstrate that the osteocytes can regulate the other cells’  
334 activity, we report the results obtained after the individual manipulation of the maximum production  
335 levels of OPG, RANKL and Scl by the osteocytes.

### 336 **Homeostatic remodeling**

337 The *in silico* simulations were able to reproduce bone remodeling with realistic changes, compared to  
338 the *in vivo* data, through single-cell mechanotransduction of the mechanical signal. Figure 3 shows a  
339 representative *in vivo* sample and *in silico* model of homeostasis. In Figure 3A, the individual  
340 normalized trabecular bone volume fraction (Norm. BV/TV) is shown for the complete original  
341 dataset, illustrating high variability within the group and for each animal over time. On the other  
342 hand, the *in silico* data of Norm. BV/TV were more stable after the initial remodeling phase. The  
343 values of  $\varepsilon$  are shown in Figure 3B with regions of high and low mechanical signal perceived by the  
344 osteocytes. *In vivo* data shows that bone formation and bone resorption occur throughout the bone  
345 microarchitecture, whereas in the *in silico* results only bone formation occurs more widely in the  
346 trabecular region, see Figure 3C. Indeed, bone resorption is more localized at the top of the trabecular  
347 region which corresponds to the distal side of the CV6 where the mechanical force is simulated.



348 Moreover, bone formation and bone resorption can alternate with each other in the same local region  
349 over time *in vivo*, whereas *in silico* bone resorption events can change their locations more frequently  
350 compared to bone formation events. The static trabecular bone parameters are shown in Figure 3D.  
351 BV/TV and Tb.Th changed over time in a similar way between the simulated data and the *in vivo*  
352 data and these two groups had a similar average (n.s. between groups and for the interaction time-  
353 group). Additionally, *in silico* Tb.Sp and Tb.N followed *in vivo* trends (n.s. for the interaction time-  
354 group). While Tb.Sp and Tb.N remained relatively constant over time *in vivo*, *in silico* we observed a  
355 significant decrease and an increase in Tb.Sp and Tb.N, respectively ( $p < 0.05$  between groups and for  
356 the interaction time-group). Additionally, we also observed an increase in BS/BV and BS/TV *in*  
357 *silico* but *in vivo* these values remain closer to their initial value ( $p < 0.05$  between groups and for the  
358 interaction time-group). MAR obtained from the *in silico* simulations was significantly lower than  
359 the *in vivo* values ( $p < 0.05$  between groups) and MRR was much higher *in silico* compared to the *in*  
360 *vivo* data ( $p < 0.05$  between groups); the values of MAR and MRR developed differently between the  
361 *in silico* and the *in vivo* groups ( $p < 0.05$  for the interaction time-group). The simulation results  
362 captured the BFR average value over time (n.s. between groups) but its temporal evolution was  
363 significantly different compared to the *in vivo* data ( $p < 0.05$  for the interaction time-group). BRR had  
364 similar values *in vivo* and *in silico* (n.s. between groups) with a similar trend over time (n.s. for the  
365 interaction time-group). On the other hand, MS and ES were lower in the *in silico* simulations  
366 compared to the *in vivo* data ( $p < 0.05$  between groups). MS presented a different temporal progression  
367 ( $p < 0.05$  for the interaction time-group) while ES did not show a significantly different temporal  
368 evolution (n.s. for the interaction time-group).

### 369 **High osteoprotegerin inhibits osteoclast resorption**

370 The variation of OPG levels produced by the osteocytes led to a change in bone remodeling activity  
371 from the cells, see Figure 4. The main effect of the spatial characterization of the remodeling regions  
372 was a higher or lower catabolic activity in the distal end of the CV6 when OPG was reduced or  
373 increased respectively, see Figure 4A. This cell activity was reflected in the Norm. BV/TV with  
374 lower values when OPG was lower and higher values when OPG was higher ( $p < 0.05$  between  
375 groups, for all possible group comparisons and for the interaction time-group), see Figure 4b. Norm.  
376 Tb.Th. showed no significant difference for the interaction time-group and in the pairwise  
377 comparison between the values obtained with high and medium OPG levels (n.s.). Norm. BS/BV  
378 showed an inverse relationship with the OPG levels ( $p < 0.05$  between groups, for all possible group  
379 comparisons). In addition, Norm. BS/BV showed different curves over time ( $p < 0.05$  for the  
380 interaction time-group). Norm. BS/TV, Norm. Tb.Sp and Norm. Tb.N were not affected by the  
381 changes in OPG levels (n.s. between groups and for the interaction time-group). BFR was not  
382 significantly affected by the variations in OPG with a similar slightly decreasing trend over time  
383 among the three levels. The BRR and ES showed a similar variability of Norm. BS/BV, with lower  
384 values when OPG was higher and higher values when OPG was lower ( $p < 0.05$  between groups, for  
385 all possible group comparisons). The significance of these changes was observed for both BRR and  
386 ES over time between groups data ( $p < 0.05$  for the interaction time-group). MS showed significantly  
387 different values between groups ( $p < 0.05$ ), however only the comparisons of high OPG-medium OPG  
388 and medium OPG-low OPG showed significant differences between the groups ( $p < 0.05$ ). MAR and  
389 MRR did not show differences among the groups when the OPG production level was changed in the  
390 simulations. These results suggest that OPG produced by the osteocytes can inhibit the osteoclasts  
391 recruitment and the consequent amount of resorption by the available osteoclasts. In addition, the  
392 number of osteoclasts also influenced the number of active osteoblasts, as shown by the variability of  
393 the MS. The net effect of these changes has an impact on the static parameters, primarily on Norm.  
394 BV/TV where the homeostatic balance is lost with alterations of the OPG levels.

### 395 **High receptor activator of nuclear factor kB ligand promotes bone resorption**

396 The variation of RANKL levels produced by the osteocytes led to a different bone remodeling  
397 activity from the osteoblasts and osteoclasts, see Figure 5. Similar to the variations observed for  
398 OPG, we observed primarily a lower or higher catabolic activity when RANKL in the distal end of  
399 the CV6 was reduced or increased respectively, see Figure 5A. This cell activity was reflected in the  
400 Norm. BV/TV, Norm. Tb.Th. with lower values when RANKL was higher and higher values when  
401 RANKL was lower ( $p < 0.05$  between groups, for all possible group comparisons and for the  
402 interaction time-group), see Figure 5B. Norm. BS/TV did respond differently to higher or lower  
403 RANKL values over time but the average values over time were not statistically significantly  
404 different (n.s. between groups and  $p < 0.05$  for the interaction time-group). Norm. BS/BV, Norm.  
405 Tb.N and BRR and ES were lower when RANKL was lower and they were higher when RANKL  
406 was higher ( $p < 0.05$  between groups, for all possible group comparisons and for the interaction time-  
407 group). Norm. Tb.Sp was not affected by the changes in RANKL over time and its average value was  
408 not affected (n.s. between groups and for the interaction time-group). The changes in RANKL had an  
409 impact on BFR, with higher or lower values when RANKL was higher or lower, respectively ( $p < 0.05$   
410 between groups and for the interaction time-group). The only comparison which did not show a  
411 significant difference in BFR was between high and medium levels of RANKL. Osteoblastic activity  
412 was also affected by the changes in RANKL in a similar way of BFR ( $p < 0.05$  between groups, for all  
413 possible group comparisons and for the interaction time-group). MAR and MRR did not show  
414 differences among the groups with changing RANKL production levels. These results suggest that  
415 RANKL promoted the osteoclasts differentiation by the changes of ES which in turn led to a  
416 variability of the resorption. The changes in the Ob recruitment are reflected in the extent of the  
417 formed surface by the Ob. The change in the formed surface had a cumulative effect on different  
418 values of BFR. The net effect of these changes had an impact on the static parameters, with the  
419 parameters starting to differ from the baseline condition earlier compared to OPG, thus augmenting  
420 the diversion from the homeostatic condition.

### 421 **High Scl blocks bone formation by inhibiting osteoblasts**

422 The variation of Scl levels produced by the osteocytes led to a different bone remodeling activity  
423 from the osteoblasts and osteoclasts compared to what was observed for the variations of RANKL  
424 and OPG before, see Figure 6. In the proximal end of the CV6 we observed primarily higher or lower  
425 anabolic activity of the osteoblasts when Scl was reduced or increased respectively, see Figure 6A.  
426 Therefore, bone formation was affected, and similar effect was observed in the Norm. BV/TV with  
427 lower values when Scl was higher, see Figure 6B. Indeed, the variations of Scl were statistically  
428 significant for Norm. BV/TV when comparing high and low Scl values as well as high and medium  
429 Scl values ( $p < 0.05$ ). However, their curves were not significantly different over time (n.s. for the  
430 interaction time-group). The statistical findings for Norm. BV/TV also apply to Norm. Tb.Th which  
431 slightly decreased over time and stabilized afterwards with a high Scl level whereas it increased when  
432 Scl was medium or lower ( $p < 0.05$  for the group comparisons high-low and high-medium).  
433 Conversely, Norm. BS/BV and Norm. BS/TV increased over time. The statistical significance of the  
434 variations for Norm BS/BV was the same as of Norm. BV/TV, whereas Norm BS/TV showed  
435 differences only in the group comparison high-medium ( $p < 0.05$ ). Interestingly, no increase in the  
436 Norm. BV/TV was observed for lower values of Scl. Norm. Tb.Sp and Norm. Tb.N did not present  
437 significant differences between the variations of Scl (n.s. between groups) and their temporal  
438 evolution between different levels (n.s. for the interaction time-group) was not significantly different  
439 statistically. BFR showed a significant variability due to Scl ( $p < 0.05$  between groups) but only in the  
440 comparisons high-low and high-medium. Also, MS was affected by the variations of Scl in a more

441 evident way ( $p < 0.05$  between groups, for all possible group comparisons). Scl did not change how  
442 bone was deposited by osteoblasts and this outcome was visible from the absence of variability in  
443 MAR with different Scl values (n.s. between groups and for the interaction time-group). BRR, MRR  
444 and ES did not show differences when Scl levels changed, nor its effect was significantly visible over  
445 time (n.s. between groups and for the interaction time-group). The changes in Scl levels had a net  
446 effect on the Norm. BV/TV less visible compared to the changes in OPG and RANKL levels, with a  
447 temporal separation from the homeostatic range of values similar to the OPG case.

## 448 Discussion

449 The proposed *in silico* micro-MPA model successfully simulated trabecular bone remodeling to  
450 evaluate the static and dynamic morphometry of the trabecular bone microarchitecture. We  
451 demonstrated that our model can simulate a homeostatic response similar to that observed with *in*  
452 *vivo* data. Although some morphological aspects were not captured by the simulations, our model  
453 showed adaptation towards a normalized trabecular bone fraction in all samples. Furthermore, the  
454 variability observed *in vivo* was also partially reflected in our simulations. Capturing the static  
455 parameters with *in silico* models has been proven to be challenging and the most frequent parameter  
456 to be captured was BV/TV (Schulte et al. 2013; Levchuk et al. 2014; Levchuk 2015). This parameter  
457 did not show significant differences on average between the *in silico* and the *in vivo* values, whereas  
458 Tb.Sp and Tb.N were different in our simulations compared to the *in vivo* data. Our simulations  
459 showed a similar evolution pattern of the static bone morphometric parameters across the samples in  
460 the second half of the simulation, meaning that it was possible to simulate similar bone changes for a  
461 group of samples with limited variability in the output. The single-cell activity and the signaling  
462 pathways were additional information modelled and they could be further tuned to capture the  
463 spatiotemporal evolution of the bone microarchitectures. This approach might be considered a step  
464 further in modeling the action of single cells and the signaling pathways compared to models of bone  
465 remodeling based on systemic ODEs where the spatial information of the cells is missing (Buenzli et  
466 al. 2012; Pastrama et al. 2018; Martin et al. 2019). The parameters of the single cells' activity can be  
467 directly linked to some parameters, e.g., MAR was correlated to the osteoblast synthesis rate of  
468 osteoid and the mineralization rate and MRR is correlated to the osteoclast resorption rate of mineral  
469 and osteoid (Supplementary Table S2). However, changing such parameters will also lead to changes  
470 in BFR and BRR as a collective effect of the cells' activity. MS and ES could also be affected by  
471 these changes to a reduced extent because those parameters can only extend or reduce the boundary  
472 of the already present remodeled regions. The amount of remodeled surface is mainly linked to the  
473 active spatial cellular distribution on the surface where the cells can remodel bone.

474 Tb.N, Tb.Th and Tb.Sp could be dependent on the apposition and resorption rates by osteoblasts and  
475 osteoclasts as well as by the mineralizing and eroded surface. The mineral apposition and resorption  
476 rates had to be higher to reduce the difference between *in silico* and *in vivo* bone formation and  
477 resorption rates, meaning that eventually the trabecular parameters would be affected by these  
478 changes by more accentuated changes in the local remodeling area. If MAR, MRR, MS and ES were  
479 closer to the *in vivo* values, the static trabecular parameters could have better followed the  
480 corresponding *in vivo* values. However, this aspect should be further inspected because, for example,  
481 the *in silico* model of Levchuk and colleagues captured Tb.N, Tb.Th and Tb.Sp despite a significant  
482 discrepancy in dynamic parameters (Levchuk et al. 2014), while the model of Schulte and colleagues  
483 for ovariectomy and loading captured some dynamic parameters and BV/TV but not Tb.N, Tb.Th and  
484 Tb.Sp (Schulte et al. 2013). The regulation of the dynamic parameters was not trivial because the  
485 mineralizing and eroded surfaces were not easy to capture due to the mechanical environment, the  
486 mechanotransduction and the subsequent cascade in the signaling process to regulate osteoblasts and

487 osteoclasts activity. The remodeled regions were rather large *in silico* compared to *in vivo* which  
488 were more scattered throughout the trabecular volume. Thus, the trabecular remodeling by the single  
489 cells was less localized *in silico*.

490 We demonstrated OPG inhibits excessive osteoclastic bone resorption as it was observed previously  
491 (Kramer et al. 2010; Cawley et al. 2020). Cawley and colleagues found OPG to be secreted by  
492 osteoblasts (Cawley et al. 2020) whereas Kramer and colleagues found osteocytes to be the cells  
493 mainly producing OPG (Kramer et al. 2010). Our work highlighted osteocytes are the cells  
494 responsible for the production of RANKL and the subsequent recruitment of osteoclasts and increase  
495 of bone resorption, as it was shown in previous works (Nakashima et al. 2011; Xiong et al. 2015). In  
496 our work, osteocytes were also identified as sources of sclerostin inhibiting the osteoblastic activity  
497 and therefore reducing bone formation. This finding was experimentally obtained also by van  
498 Bezooijen and colleagues (Van Bezooijen et al. 2004), where sclerostin protein was found to be  
499 expressed by osteocytes and not by osteoclasts in cortical and trabecular bone. Further, they also  
500 observed the inhibitory effect of sclerostin on osteoblasts, confirming its importance for regulating  
501 bone formation (Winkler et al. 2003; Li et al. 2008; Colucci et al. 2011).

502 We observed that affecting the catabolic response would also imply a change in the anabolic activity.  
503 This aspect was evident from the variations of RANKL and OPG which had a direct impact on the  
504 osteoclasts' activity, but the osteoblasts' activity was subsequently affected by that. On the other  
505 hand, the anti-anabolic response would also imply a subsequent change in the catabolic activity, as it  
506 was seen from the variations of Scl which inhibited osteoblasts and a consequent slower resorption  
507 activity. These findings confirm the existence of the coupling between bone formation and bone  
508 resorption events as observed *in vivo*. Our *in silico* model represented bone formation mostly  
509 occurring over time in the same region where the strains were high, until the osteoblasts back  
510 differentiated into lining cells or became embedded into the osteoid and differentiate into  
511 preosteocytes. On the other hand, bone resorption occurred starting from a region where the strains  
512 were low because in this region RANKL was higher and osteoclasts were mainly recruited here.  
513 TGF- $\beta$ 1 is thought to be responsible for coupling bone resorption and bone formation (Raggatt and  
514 Partridge 2010; Kasagi and Chen 2013; Weivoda et al. 2016; Durdan et al. 2021) and osteoclasts  
515 resorb bone in regions of low strains. MSCs proliferated closer to osteoclasts due to the presence of  
516 TGF- $\beta$ 1 being released upon resorption in these regions of low strains. In addition, in such regions,  
517 sclerostin was also produced by osteocytes to inhibit bone formation by the osteoblasts. Therefore,  
518 the osteoblastic differentiation of such cells was inhibited and MSCs would directly differentiate into  
519 lining cells instead of osteoblasts in these regions of low strains. Moreover, we included the  
520 production of RANKL and OPG by osteoblasts and lining cells and their production levels  
521 confluence in the total levels of OPG and RANKL. An extensive calibration of the coupling would  
522 dramatically scale the number of simulations required to calibrate all these aspects. Such calibration  
523 should include the simulation of bone formation regions occurring over subsequent bone resorption  
524 areas and vice versa as observed *in vivo*. It is still not clear how the cells are able to have this fast  
525 (bi)weekly turnover of events in place when their lifespan in mice is relatively longer, e.g., at least  
526 two weeks (Søe 2020). These complex dynamics remain to be further elucidated.

527 It is not yet fully understood when the osteoclasts stop resorbing bone (Filgueira 2010), but it is  
528 assumed that this happens when the mineral phase of the bone underneath is degraded to a certain  
529 extent (Kanehisa and Heersche 1988). Currently, this mechanism is not reproduced directly in the *in*  
530 *silico* model. In addition, it was observed that collagen can decelerate the demineralization activity  
531 when osteoclasts resorb bone in pit mode, protecting bone against excessive resorption (Delaisse et  
532 al. 2021). In our *in silico* model, osteoclasts stopped being active, and therefore resorptive, when they



533 were not in a cluster or if they died by apoptosis or due to lack of bound RANK receptors. Further,  
534 the resorption rate of mineral and collagen by osteoclasts was considered the same. This is the case  
535 when osteoclasts resorb bone in trench mode (Delaisse et al. 2021). On the other hand, these rates are  
536 usually different when osteoclasts resorb bone in pit mode, with solubilization of mineral being faster  
537 than the evacuation of collagen fragments (Delaisse et al. 2021). The modelling of these events might  
538 be an oversimplification of how osteoclasts stop being active and it does not represent the same  
539 frequency of interruption of bone resorption by osteoclasts.

540 For initializing the cytokines in the model, we used values measured from experimental studies  
541 which are closely in line with the modelled environment. However, it is likely that the values  
542 appropriate for the mouse vertebra at a given age might differ from the experimental values due to  
543 site, age, loading and phenotypic characterization of the data. This problem has been identified for *in*  
544 *silico* models of bone mechanobiology (Checa and Prendergast 2009), where simple approaches were  
545 adopted to overcome this lack of information (Perier-Metz et al. 2020, 2022; Borgiani et al. 2021).  
546 This limitation might be partially overcome by taking advantage of the mechanical environment as it  
547 was performed by Tourolle and colleagues (Tourolle et al. 2021). A more synergistic study where the  
548 cytokines are experimentally obtained from the same site on a regular basis would help in the  
549 calibration of this micro-MPA *in silico* model. In addition, the information on the cell densities is  
550 scarce and they might change between different bones, age, sex, and physiological conditions.  
551 Moreover, the cells might be distributed differently in bone and in the marrow. This aspect is  
552 especially relevant for osteocytes which are not motile in bone, meaning that their initial distribution  
553 is essentially preserved throughout the time of the simulation, except when they are no longer present  
554 due to cell apoptosis or bone resorption. The initial cell densities and cytokine distributions will have  
555 implications in the estimations of the proliferation and cell rates as well as the single-cell activity,  
556 e.g., resorption and cytokine production rates. Consequently, the amount of unknown initial  
557 conditions is very high, and it can take some time before the simulated cells and cytokines can reach  
558 a spatio-temporal distribution which is more realistic and not affected by the assumed initial  
559 condition. This limitation was addressed by the additional iterations of the model first without  
560 changes and then with changes to the bone microarchitecture. However, the number of iterations  
561 required for this purpose could be even higher.

562 The receptor-ligand kinetics in the context of micro-MPA *in silico* models is still very novel and  
563 needs further exploration. Depending on the application, the formulations might differ to include  
564 other aspects like trafficking and intracellular signaling (Cilfone et al. 2015). Moreover, there might  
565 be molecular aspects that might be lost when using this kind of equation and coefficients might be  
566 recalibrated depending on the environment. Indeed, some coefficients might be experimentally  
567 obtained from analysis of the interactions between monomers (Nelson et al. 2012), but their usage  
568 might not be straightforward due to the coexistence of other phenomena like spatial diffusion and  
569 movement of the ligands from one receptor to the other in the proximity of the cell surface (Erbaş et  
570 al. 2019). Furthermore, the cell response is usually achieved when most of its surface receptors are  
571 still unoccupied (Lodish et al. 1999). It is still difficult to estimate *in vivo* the number of surface  
572 receptors and the number of occupied receptors along with an accurate description of the receptor-  
573 ligand kinetics, especially when competitive reactions are involved, e.g., the RANKL-RANK-OPG  
574 axis. Hence, the receptor-ligand kinetics in bone remodeling remains challenging but crucial. *In silico*  
575 models of bone remodeling use this information to regulate cell fate and differentiation by  
576 parametrization of the coefficients used in the equations as well as the number of receptors per cell.  
577 These factors are relevant at the cellular and gene scales that influence bone remodeling activities in  
578 the whole volume. The numerical estimates are a starting point, but it is advisable to employ  
579 experimental values detected from receptors on (bone remodeling) cells presenting such receptors.

580 Different experimental approaches directly applied to the cells (Warren et al. 2015) or in a  
581 multidimensional environment (Chesla et al. 1998) might help in estimating the coefficients to be  
582 used for modelling such phenomena *in silico*.

### 583 **Conclusion**

584 This work showcases the use of single-cell mechanotransduction in a micro-MPA *in silico* model of  
585 trabecular bone remodeling applied to *in vivo* data. We were able to reproduce homeostatic bone  
586 remodeling and highlight how tuning the single-cell osteocyte production rates of OPG, RANKL and  
587 Scl further induces anabolic, anti-anabolic, catabolic and anticatabolic responses from the baseline  
588 model. The calibration with bone morphometric parameters was used in this work, however, it would  
589 be helpful to employ a complete experimental dataset which can be directly assigned to the  
590 parameters of the model, e.g., serum markers and cellular properties. By careful calibration of  
591 biological parameters, we hope this model shed light on bone remodeling and associated diseased  
592 states. Micro-MPA models over several scales will be needed in the future because only with them it  
593 will be possible to unravel biological processes and their effects realistically. This will advance the  
594 field of bone remodeling and our current understanding of its mechanisms.

### 595 **Conflict of Interest**

596 *The authors declare that the research was conducted in the absence of any commercial or financial*  
597 *relationships that could be construed as a potential conflict of interest.*

### 598 **Author Contributions**

599 DB, FM, CL, JK, YDB, FS and RM contributed to the design of the study. DAB, FM, CL and JK  
600 contributed to the development of the model, assembly and assessment of data, AS and FS  
601 contributed to the statistical analysis and interpretation of results, DB, FS, YDB and RM wrote the  
602 main manuscript text. All authors contributed to revising the manuscript and approved the final  
603 version to be submitted.

### 604 **Funding**

605 This work was funded by the European Research Council (ERC Advanced MechAGE ERC-2016-  
606 ADG-741883).

### 607 **Acknowledgments**

608 This work was supported by a grant from the Swiss National Supercomputing Centre (CSCS) under  
609 project ID s1070.

### 610 **References**

- 611 Bezooijen RL Van, Roelen BA, Visser A, *et al.* 2004. Sclerostin is an osteocyte-expressed negative  
612 regulator of bone formation, but not a classical BMP antagonist. *The Journal of experimental*  
613 *medicine* **199**: 805–14.  
614  
615  
616 Boaretti D, Betts DC, and Müller R. 2018. Studying how the link between mechanical stimulation  
617 and cellular activation effects bone microarchitecture. In: Book of Abstracts of the 25th Congress

- 618 of the European Society of Biomechanics (ESB 2019).  
619  
620  
621 Boaretti D, Wehrle E, Bansod Y, *et al.* 2022. Perspectives on in silico bone mechanobiology:  
622 computational modelling of multicellular systems. *European Cells and Materials* **44**: 56–73.  
623  
624  
625 Borgiani E, Duda GN, Willie BM, and Checa S. 2021. Bone morphogenetic protein 2-induced  
626 cellular chemotaxis drives tissue patterning during critical-sized bone defect healing: an in silico  
627 study. *Biomechanics and Modeling in Mechanobiology*: 1–18.  
628  
629  
630 Bourhis E, Wang W, Tam C, *et al.* 2011. Wnt antagonists bind through a short peptide to the first  $\beta$ -  
631 propeller domain of LRP5/6. *Structure* **19**: 1433–42.  
632  
633  
634 Boyce BF and Xing L. 2008. Functions of RANKL/RANK/OPG in bone modeling and remodeling.  
635 *Archives of biochemistry and biophysics* **473**: 139–46.  
636  
637  
638 Buenzli PR, Pivonka P, Gardiner BS, and Smith DW. 2012. Modelling the anabolic response of bone  
639 using a cell population model. *Journal of theoretical biology* **307**: 42–52.  
640  
641  
642 Cawley KM, Bustamante-Gomez NC, Guha AG, *et al.* 2020. Local production of osteoprotegerin by  
643 osteoblasts suppresses bone resorption. *Cell Rep* **32**: 108052.  
644  
645  
646 Checa S and Prendergast PJ. 2009. A mechanobiological model for tissue differentiation that includes  
647 angiogenesis: a lattice-based modeling approach. *Annals of biomedical engineering* **37**: 129–45.  
648  
649  
650 Chesla SE, Selvaraj P, and Zhu C. 1998. Measuring two-dimensional receptor-ligand binding kinetics  
651 by micropipette. *Biophysical journal* **75**: 1553–72.  
652  
653  
654 Cilfone NA, Kirschner DE, and Linderman JJ. 2015. Strategies for efficient numerical  
655 implementation of hybrid multi-scale agent-based models to describe biological systems. *Cellular  
656 and molecular bioengineering* **8**: 119–36.  
657  
658  
659 Colucci S, Brunetti G, Oranger A, *et al.* 2011. Myeloma cells suppress osteoblasts through sclerostin  
660 secretion. *Blood Cancer J* **1**: e27–e27.  
661  
662  
663 Dalcin LD, Paz RR, Kler PA, and Cosimo A. 2011. Parallel distributed computing using Python. *Adv  
664 Water Resour* **34**: 1124–39.  
665  
666

- 667 Delaisse J-M, S e K, Andersen TL, *et al.* 2021. The mechanism switching the osteoclast from short  
668 to long duration bone resorption. *Frontiers in Cell and Developmental Biology* **9**: 555.  
669  
670
- 671 Demidov D. 2019. AMGCL: An efficient, flexible, and extensible algebraic multigrid  
672 implementation. *Lobachevskii Journal of Mathematics* **40**: 535–46.  
673  
674
- 675 Dobson PF, Dennis EP, Hipps D, *et al.* 2020. Mitochondrial dysfunction impairs osteogenesis,  
676 increases osteoclast activity, and accelerates age related bone loss. *Sci Rep* **10**: 1–14.  
677  
678
- 679 Durdan MM, Azaria RD, and Weivoda MM. 2021. Novel insights into the coupling of osteoclasts  
680 and resorption to bone formation. In: *Seminars in Cell & Developmental Biology*.  
681  
682
- 683 Elson A, Anuj A, Barnea-Zohar M, and Reuven N. 2022. The origins and formation of bone-  
684 resorbing osteoclasts. *Bone*: 116538.  
685  
686
- 687 Erbař A, La Cruz MO De, and Marko JF. 2019. Receptor-ligand rebinding kinetics in confinement.  
688 *Biophysical journal* **116**: 1609–24.  
689  
690
- 691 Filgueira L. 2010. Osteoclast differentiation and function. In: *Bone Cancer*. Elsevier.  
692  
693
- 694 Flaig C and Arbenz P. 2011. A scalable memory efficient multigrid solver for micro-finite element  
695 analyses based on CT images. *Parallel Computing* **37**: 846–54.  
696  
697
- 698 Franz-Odendaal TA, Hall BK, and Witten PE. 2006. Buried alive: how osteoblasts become  
699 osteocytes. *Developmental dynamics: an official publication of the American Association of*  
700 *Anatomists* **235**: 176–90.  
701  
702
- 703 Hildebrand T, Laib A, M ller R, *et al.* 1999. Direct three-dimensional morphometric analysis of  
704 human cancellous bone: microstructural data from spine, femur, iliac crest, and calcaneus. *Journal*  
705 *of bone and mineral research* **14**: 1167–74.  
706  
707
- 708 Jakob W, Rhinelander J, and Moldovan D. 2017. pybind11 - Seamless operability between C++11  
709 and Python.  
710  
711
- 712 Kanehisa J and Heersche J. 1988. Osteoclastic bone resorption: in vitro analysis of the rate of  
713 resorption and migration of individual osteoclasts. *Bone* **9**: 73–9.  
714  
715



- 716 Kanis JA, Norton N, Harvey NC, *et al.* 2021. SCOPE 2021: a new scorecard for osteoporosis in  
717 Europe. *Archives of osteoporosis* **16**: 1–82.  
718  
719
- 720 Kasagi S and Chen W. 2013. TGF-beta1 on osteoimmunology and the bone component cells. *Cell &*  
721 *Bioscience* **3**: 1–7.  
722  
723
- 724 Klein-Nulend J, Bacabac R, and Bakker A. 2012. Mechanical loading and how it affects bone cells:  
725 the role of the osteocyte cytoskeleton in maintaining our skeleton. *European Cells and Materials*  
726 **24**: 278–91.  
727  
728
- 729 Klein-Nulend J, Bakker AD, Bacabac RG, *et al.* 2013. Mechanosensation and transduction in  
730 osteocytes. *Bone* **54**: 182–90.  
731  
732
- 733 Kramer I, Halleux C, Keller H, *et al.* 2010. Osteocyte Wnt/ $\beta$ -catenin signaling is required for  
734 normal bone homeostasis. *Molecular and cellular biology* **30**: 3071–85.  
735  
736
- 737 Krishnan V, Bryant HU, and MacDougald OA. 2006. Regulation of bone mass by Wnt signaling. *J*  
738 *Clin Invest* **116**: 1202–9.  
739  
740
- 741 Kujoth GC, Hiona A, Pugh TD, *et al.* 2005. Mitochondrial DNA mutations, oxidative stress, and  
742 apoptosis in mammalian aging. *Science (80- )* **309**: 481–4.  
743  
744
- 745 Kuznetsova A, Brockhoff PB, and Christensen RH. 2017. lmerTest package: tests in linear mixed  
746 effects models. *Journal of statistical software* **82**: 1–26.  
747  
748
- 749 Lambers FM, Schulte FA, Kuhn G, *et al.* 2011. Mouse tail vertebrae adapt to cyclic mechanical  
750 loading by increasing bone formation rate and decreasing bone resorption rate as shown by time-  
751 lapsed in vivo imaging of dynamic bone morphometry. *Bone* **49**: 1340–50.  
752  
753
- 754 Lenth RV. 2022. emmeans: Estimated Marginal Means, aka Least-Squares Means.  
755  
756
- 757 Levchuk A. 2015. In Silico Investigation of Bone Adaptation in Health and Disease.  
758  
759
- 760 Levchuk A, Zwahlen A, Weigt C, *et al.* 2014. The Clinical Biomechanics Award 2012—presented by  
761 the European Society of Biomechanics: large scale simulations of trabecular bone adaptation to  
762 loading and treatment. *Clinical biomechanics* **29**: 355–62.  
763  
764

- 765 Li X, Ominsky MS, Niu Q-T, *et al.* 2008. Targeted deletion of the sclerostin gene in mice results in  
766 increased bone formation and bone strength. *Journal of Bone and Mineral Research* **23**: 860–9.  
767  
768
- 769 Li X, Zhang Y, Kang H, *et al.* 2005. Sclerostin binds to LRP5/6 and antagonizes canonical Wnt  
770 signaling. *Journal of Biological Chemistry* **280**: 19883–7.  
771  
772
- 773 Lin C, Jiang X, Dai Z, *et al.* 2009. Sclerostin mediates bone response to mechanical unloading  
774 through antagonizing Wnt/ $\beta$ -catenin signaling. *Journal of bone and mineral research* **24**:  
775 1651–61.  
776  
777
- 778 Lodish H, Berk A, Zipursky L, *et al.* 1999. Identification and Purification of Cell-Surface Receptors.  
779 *Molecular Cell Biology*, WH Freeman, New York,.  
780  
781
- 782 Martin M, Sansalone V, Cooper DM, *et al.* 2019. Mechanobiological osteocyte feedback drives  
783 mechanostat regulation of bone in a multiscale computational model. *Biomechanics and modeling*  
784 *in mechanobiology* **18**: 1475–96.  
785  
786
- 787 Mullender M, Huiskes R, Versleyen H, and Buma P. 1996. Osteocyte density and histomorphometric  
788 parameters in cancellous bone of the proximal femur in five mammalian species. *Journal of*  
789 *Orthopaedic Research* **14**: 972–9.  
790  
791
- 792 Nakahama K. 2010. Cellular communications in bone homeostasis and repair. *Cellular and*  
793 *molecular life sciences* **67**: 4001–9.  
794  
795
- 796 Nakashima T, Hayashi M, Fukunaga T, *et al.* 2011. Evidence for osteocyte regulation of bone  
797 homeostasis through RANKL expression. *Nature medicine* **17**: 1231–4.  
798  
799
- 800 Nelson CA, Warren JT, Wang MW-H, *et al.* 2012. RANKL employs distinct binding modes to  
801 engage RANK and the osteoprotegerin decoy receptor. *Structure* **20**: 1971–82.  
802  
803
- 804 Pastrama M-I, Scheiner S, Pivonka P, and Hellmich C. 2018. A mathematical multiscale model of  
805 bone remodeling, accounting for pore space-specific mechanosensation. *Bone* **107**: 208–21.  
806  
807
- 808 Perier-Metz C, Cipitria A, Hutmacher DW, *et al.* 2022. An in silico model predicts the impact of  
809 scaffold design in large bone defect regeneration. *Acta Biomaterialia*.  
810  
811
- 812 Perier-Metz C, Duda GN, and Checa S. 2020. Mechano-biological computer model of scaffold-  
813 supported bone regeneration: effect of bone graft and scaffold structure on large bone defect tissue

- 814       patterning. *Frontiers in Bioengineering and Biotechnology* **8**: 1245.  
815  
816
- 817       Raggatt LJ and Partridge NC. 2010. Cellular and molecular mechanisms of bone remodelling.  
818       *Journal of Biological Chemistry*: jbc-R109.  
819  
820
- 821       Rauner M, Jähn K, Hemmatian H, *et al.* 2020. Cardiovascular Calcification and Bone Mineralization.  
822       In: Cellular Contributors to Bone Homeostasis. Springer.  
823  
824
- 825       Rodan GA. 1998. Bone homeostasis. *Proceedings of the National Academy of Sciences* **95**: 13361–2.  
826  
827
- 828       Santos A, Bakker AD, and Klein-Nulend J. 2009. The role of osteocytes in bone  
829       mechanotransduction. *Osteoporosis international* **20**: 1027–31.  
830  
831
- 832       Scheuren AC, D’Hulst G, Kuhn GA, *et al.* 2020a. Hallmarks of frailty and osteosarcopenia in  
833       prematurely aged PolgA (D257A/D257A) mice. *J Cachexia Sarcopenia Muscle* **11**: 1121–40.  
834  
835
- 836       Scheuren AC, Kuhn GA, and Müller R. 2020b. Effects of long-term in vivo micro-CT imaging on  
837       hallmarks of osteopenia and frailty in aging mice. *PLoS One* **15**: e0239534.  
838  
839
- 840       Schulte FA, Zwahlen A, Lambers FM, *et al.* 2013. Strain-adaptive in silico modeling of bone  
841       adaptation - A computer simulation validated by in vivo micro-computed tomography data. *Bone*  
842       **52**: 485–92.  
843  
844
- 845       Shahnazari M, Dwyer D, Chu V, *et al.* 2012. Bone turnover markers in peripheral blood and marrow  
846       plasma reflect trabecular bone loss but not endocortical expansion in aging mice. *Bone* **50**: 628–  
847       37.  
848  
849
- 850       Søe K. 2020. Osteoclast Fusion: Physiological Regulation of Multinucleation through  
851       Heterogeneity—Potential Implications for Drug Sensitivity. *International Journal of Molecular*  
852       *Sciences* **21**: 7717.  
853  
854
- 855       Strang G. 1968. On the construction and comparison of difference schemes. *SIAM journal on*  
856       *numerical analysis* **5**: 506–17.  
857  
858
- 859       Tang Y, Wu X, Lei W, *et al.* 2009. TGF- $\beta$ 1-induced migration of bone mesenchymal stem  
860       cells couples bone resorption with formation. *Nature medicine* **15**: 757–65.  
861  
862

- 863 Tourolle D. 2019. A Micro-scale Multiphysics Framework for Fracture Healing and Bone  
864 Remodelling. *ETH Zurich Research Collection*.
- 865  
866  
867 Tourolle DC, Dempster DW, Ledoux C, *et al.* 2021. Ten-Year Simulation of the Effects of  
868 Denosumab on Bone Remodeling in Human Biopsies. *JBMR plus* **5**: e10494.
- 869  
870  
871 Trifunovic A, Wredenberg A, Falkenberg M, *et al.* 2004. Premature ageing in mice expressing  
872 defective mitochondrial DNA polymerase. *Nature* **429**: 417–23.
- 873  
874  
875 Warren JT, Zou W, Decker CE, *et al.* 2015. Correlating RANK ligand/RANK binding kinetics with  
876 osteoclast formation and function. *Journal of cellular biochemistry* **116**: 2476–83.
- 877  
878  
879 Webster DJ, Morley PL, Lenthe GH van, and Müller R. 2008. A novel *in vivo* mouse model for  
880 mechanically stimulated bone adaptation—a combined experimental and computational validation  
881 study. *Comput Methods Biomech Biomed Engin* **11**: 435–41.
- 882  
883  
884 Weivoda MM, Ruan M, Pederson L, *et al.* 2016. Osteoclast TGF- $\beta$  receptor signaling induces  
885 Wnt1 secretion and couples bone resorption to bone formation. *Journal of Bone and Mineral*  
886 *Research* **31**: 76–85.
- 887  
888  
889 Winkler DG, Sutherland MK, Geoghegan JC, *et al.* 2003. Osteocyte control of bone formation via  
890 sclerostin, a novel BMP antagonist. *The EMBO journal* **22**: 6267–76.
- 891  
892  
893 Xiong J, Piemontese M, Onal M, *et al.* 2015. Osteocytes, not osteoblasts or lining cells, are the main  
894 source of the RANKL required for osteoclast formation in remodeling bone. *PLoS One* **10**:  
895 e0138189.
- 896  
897  
898

## 899 **Figure captions**

### 900 **Figure 1**

901 Experimental design of the *in vivo* data used for the simulations of the *in silico* model. **(A)** Weekly  
902 micro-computed tomography (micro-CT) images of the sixth caudal vertebra of PolgA<sup>(D257A/D257A)</sup>  
903 mice. Half of the vertebra is shown with transparency of the cortical region over time for each  
904 measurement. **(B)** The normalized trabecular bone volume fraction slightly decreased over the course  
905 of the study in the group of mice (n=9).



906 **Figure 2**

907 The concept of the micro-MPA *in silico* model in the mouse vertebra. **(A)** The cells and cytokines  
908 modeled in the bone remodeling version of the model. **(B)** Overview of the simulation pipeline from  
909 the input data to the end of the simulation. **(C)** A schematic representation of the cell receptor-ligand  
910 kinetics modelled *in silico*. Here, the ligand can bind only to the targeted cell receptor with a forward  
911 rate  $k^f$  and it can dissociate from the receptor with a backward rate  $k^r$ . This is an example of the  
912 modelled receptor-ligand kinetics of Lipoprotein receptor-related protein 5/6 (LRP5/6)-sclerostin for  
913 an osteoblast, lining cell and mesenchymal stem cell. **(D)** A 2D slice from the trabecular region of an  
914 *in silico* simulation with osteocytes (black), osteoclasts (purple), preosteoclasts (blue), osteoblasts  
915 (orange), mesenchymal stem cells (green) and hematopoietic stem cells (brown). **(E)** A snapshot of  
916 the initial configuration of the *in silico* simulation at  $t=0$ . On the left, the osteoblasts (orange),  
917 osteoclasts (purple) and preosteoclasts (blue) are shown on the trabecular bone surface, in the middle  
918 the spatial distribution of the receptor activator of nuclear factor  $\kappa$ B (RANK) binding site occupancy  
919 on the osteoclasts and preosteoclasts and on the right the spatial distribution of the RANK ligand  
920 (RANKL) configuration in the trabecular region.

921 **Figure 3**

922 The *in vivo* data and the comparison against the *in silico* modeling of homeostasis. **(A)** The  
923 normalized bone volume fraction (Norm. BV/TV) for the complete group of mice *in vivo* (left,  $n=10$ )  
924 and for the group of mice analyzed *in silico* (right,  $n=5$ ). **(B)** Mechanical signal in the trabecular  
925 region for the representative mouse (number 5). **(C)** Bone formation, quiescent and resorption events  
926 images over time *in vivo* and *in silico*. **(D)** Static and dynamic bone morphometry values for the *in*  
927 *vivo* and *in silico* groups. In these plots, only the same selection of mice was plotted for both the *in*  
928 *vivo* and *in silico* data ( $n=5$ ).

929 **Figure 4**

930 *In silico* results of variations of the maximum single cell production level of osteoprotegerin (OPG)  
931 by osteocytes. **(A)** Biweekly FQR regions of results obtained with higher and lower OPG production  
932 levels for the representative mouse (number 5). **(B)** Static and dynamic bone morphometry parameters  
933 of the results of the simulations of the same group of mice ( $n=5$ ) under three different production  
934 levels of OPG, starting from the same initial condition of the medium level. High=higher production  
935 level of OPG, Baseline=medium production level of OPG as in the homeostatic configuration,  
936 low=lower production level of OPG.

937 **Figure 5**

938 *In silico* results of variations of the maximum single cell production level of receptor activator of  
939 nuclear factor  $\kappa$ B ligand (RANKL) by osteocytes. **(A)** Biweekly FQR regions of results obtained with  
940 higher and lower RANKL production levels for the representative mouse (number 5). **(B)** Static and  
941 dynamic bone morphometry parameters of the results of the simulations of the same group of mice  
942 ( $n=5$ ) under three different production levels of RANKL, starting from the same initial condition of  
943 the medium level. High=higher production level of RANKL, Baseline=medium production level of  
944 RANKL as in the homeostatic configuration, low=lower production level of RANKL.

945 **Figure 6**

946 *In silico* results of variations of the maximum single cell production level of sclerostin (Scl) by  
947 osteocytes. **(A)** Biweekly FQR regions of results obtained with higher and lower Scl production  
948 levels for the representative mouse (number 5). **(B)** Static and dynamic bone morphometry  
949 parameters of the results of the simulations of the same group of mice (n=5) under three different  
950 production levels of Scl, starting from the same initial condition of the medium level. High=higher  
951 production level of Scl, Baseline=medium production level of Scl as in the homeostatic  
952 configuration, low=lower production level of Scl.

953 **Supplementary Material**

954 See additional file for Supplementary Material.

955 **Data Availability Statement**

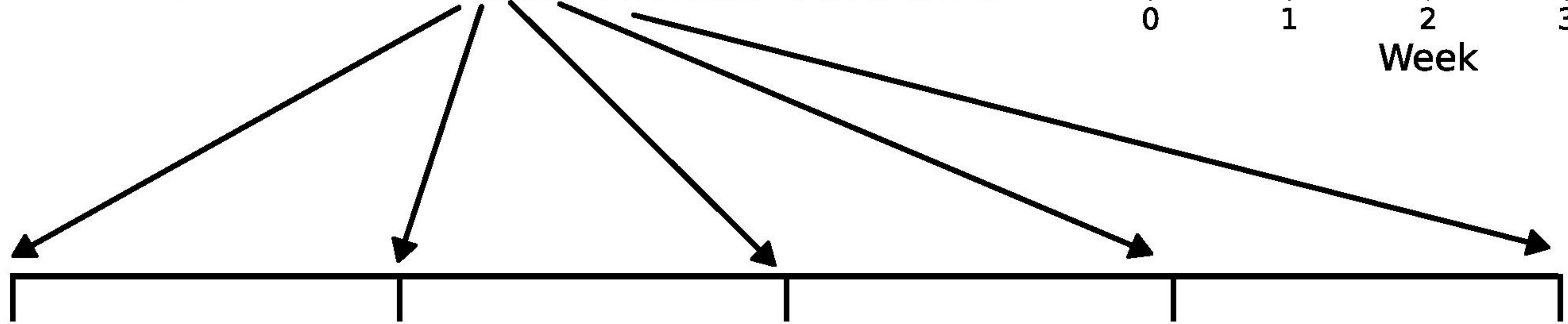
956 The raw data supporting the conclusions of this article will be made available by the authors, without  
957 undue reservation.



a)



6th caudal vertebra



m1

m2

m3

m4

m5

micro-CT

micro-CT

micro-CT

micro-CT

micro-CT

Age=38 weeks

Age=39 weeks

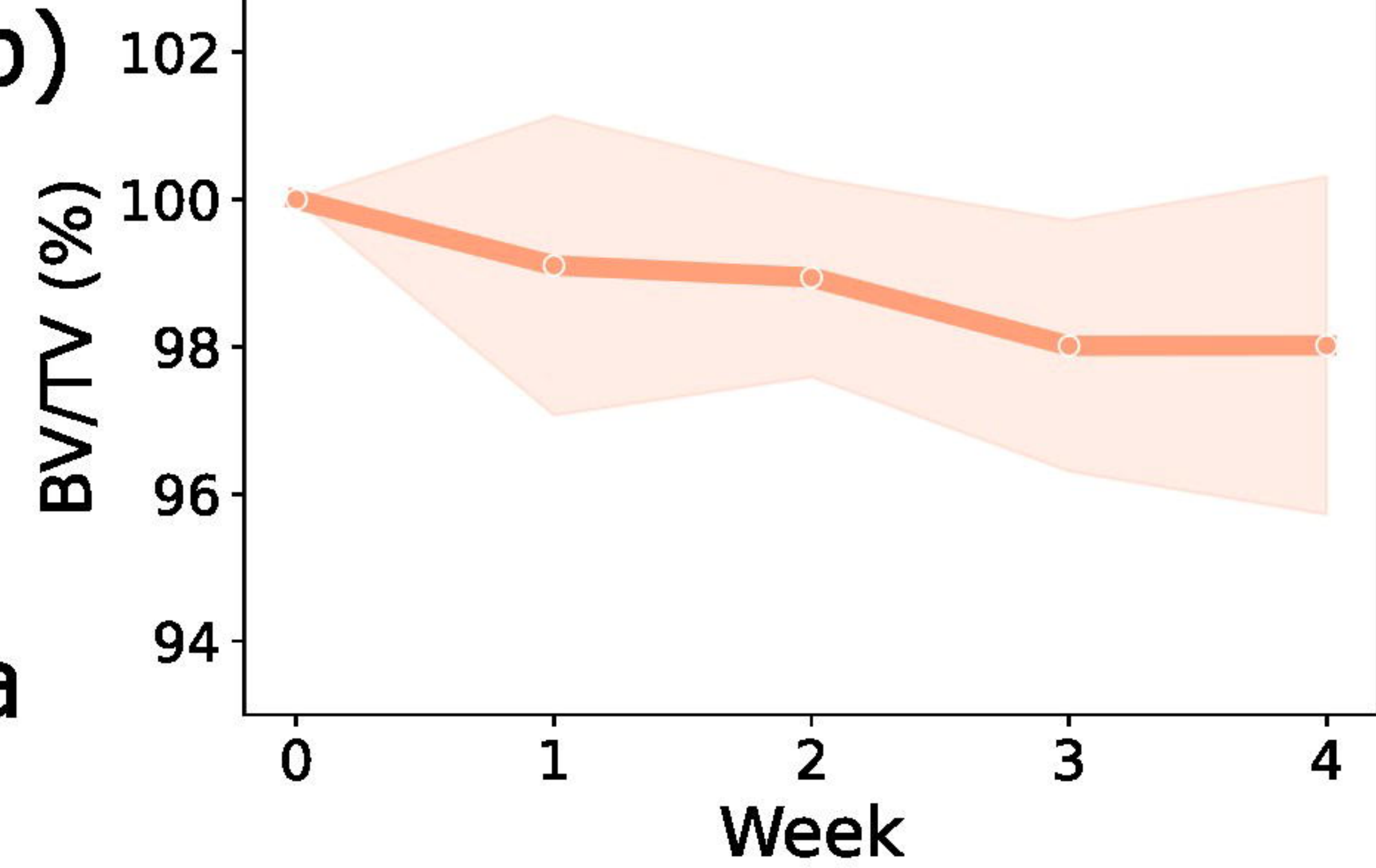
Age=40 weeks

Age=41 weeks

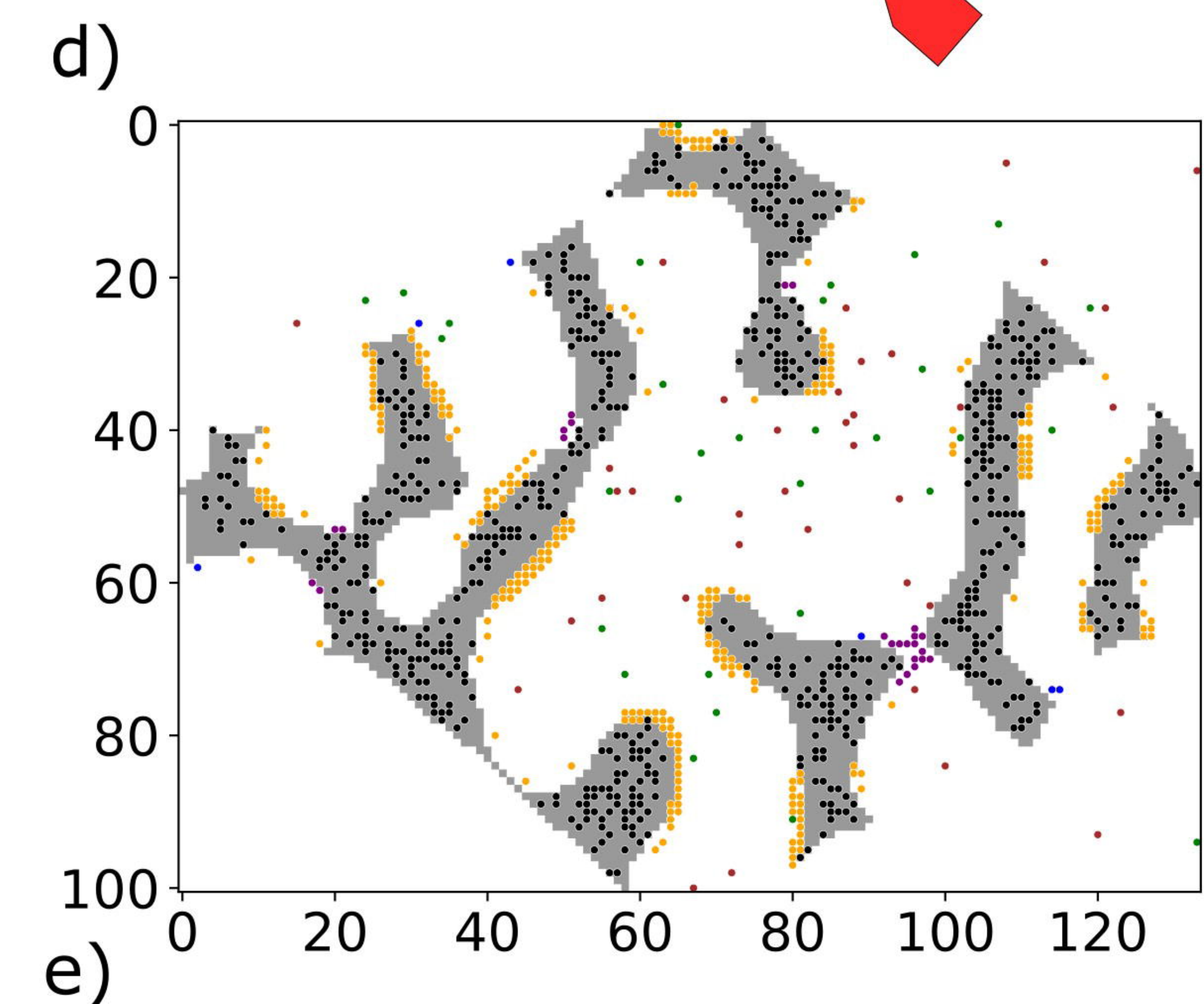
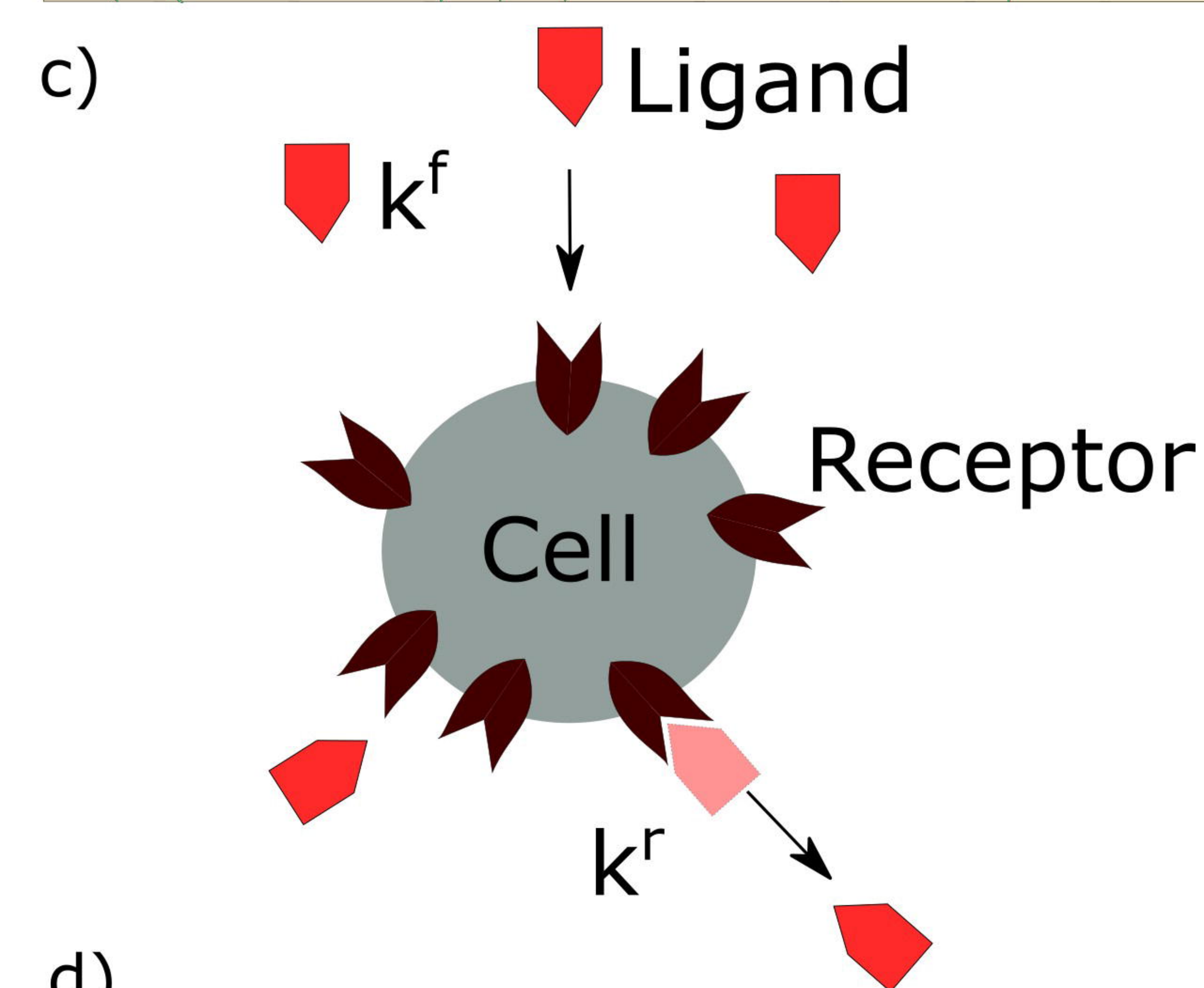
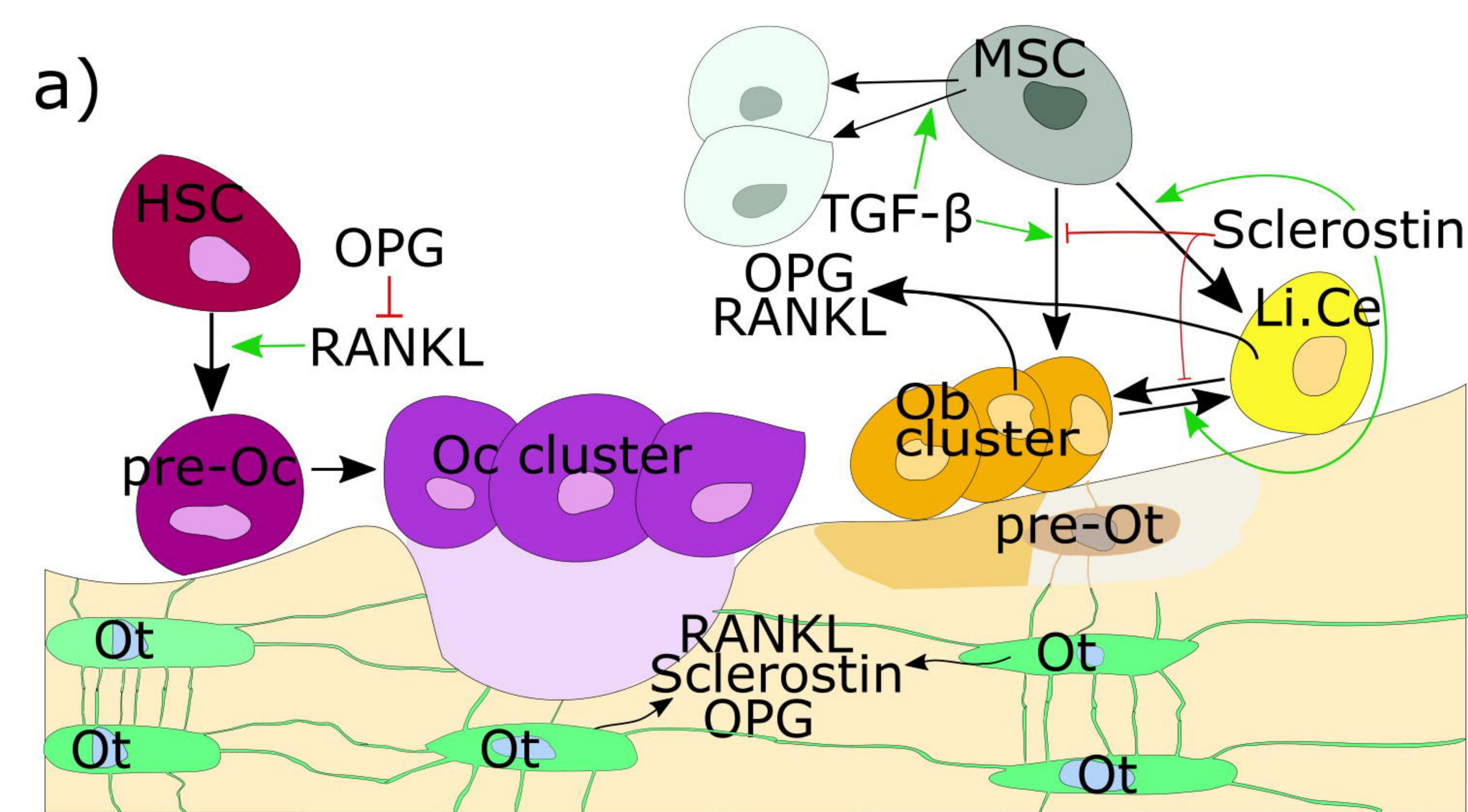
Age=42 weeks



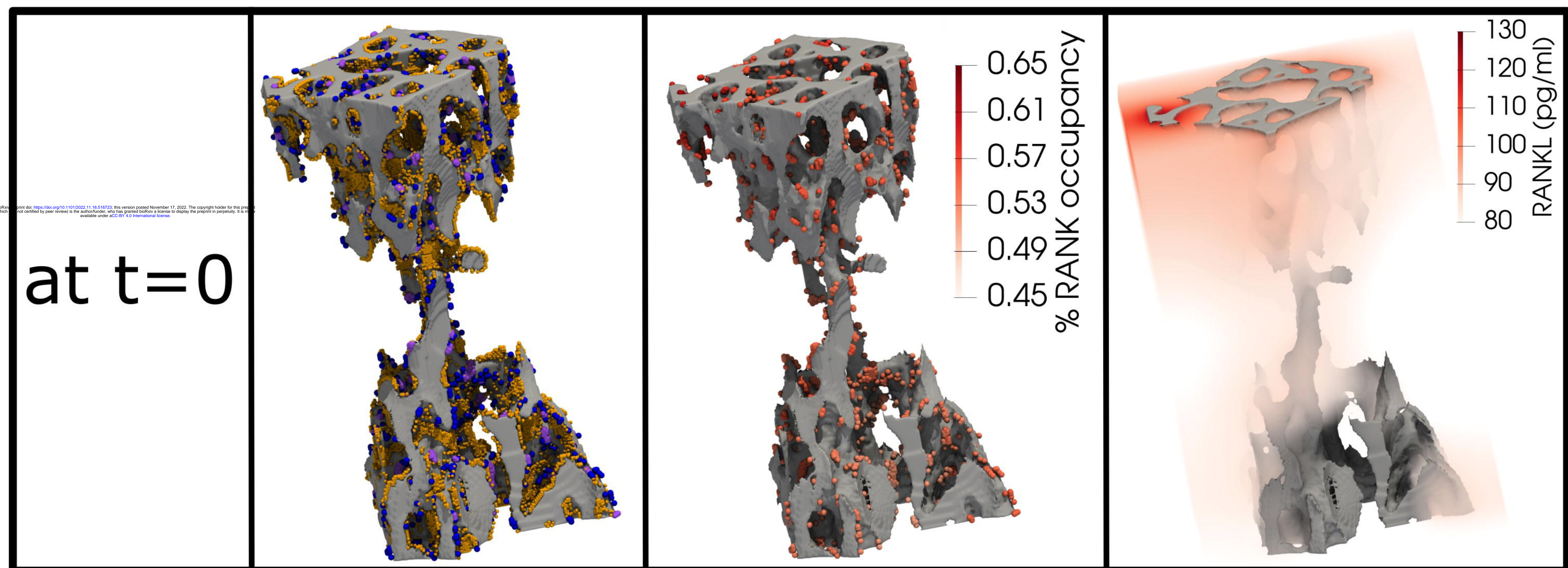
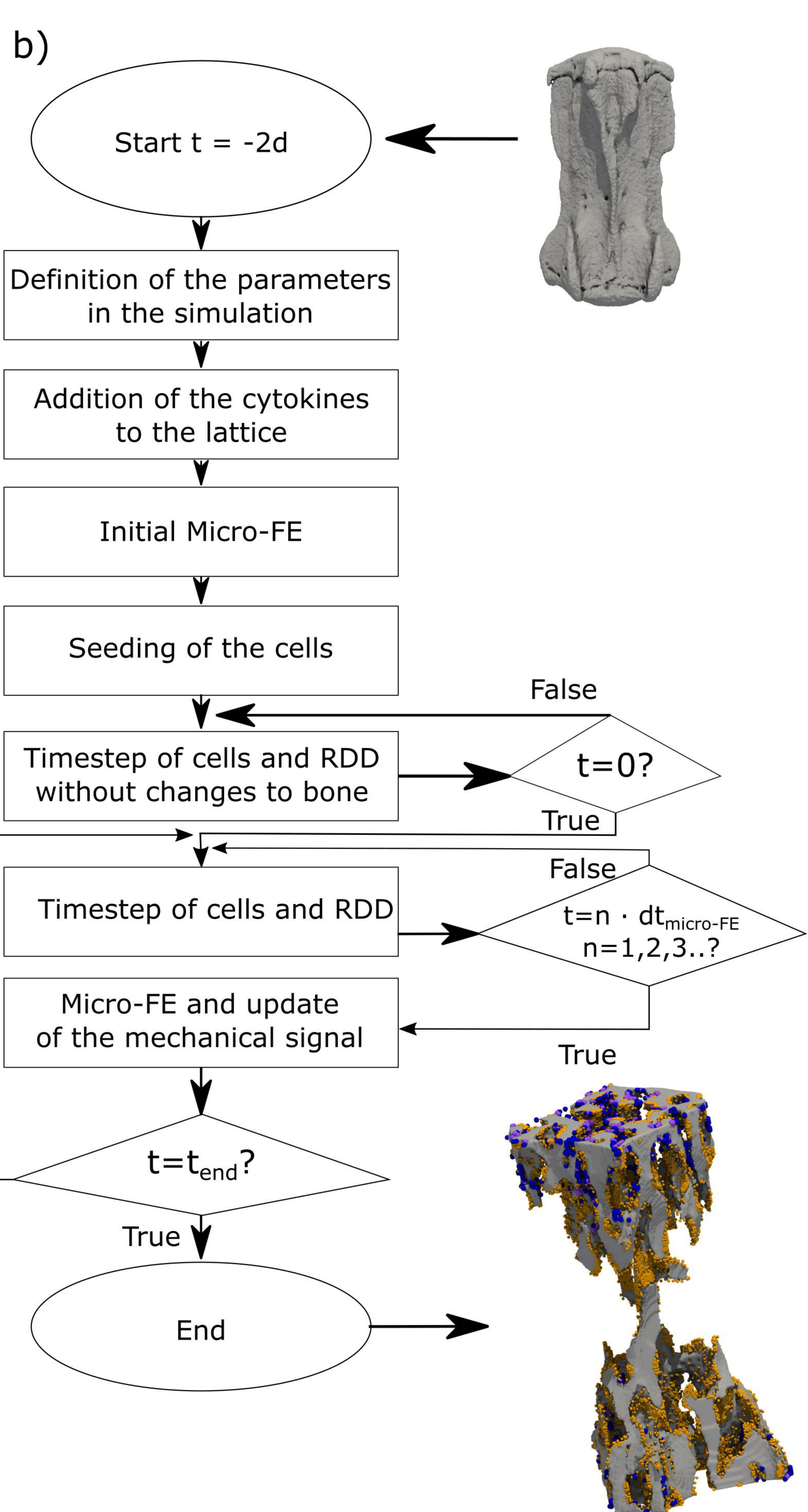
b)



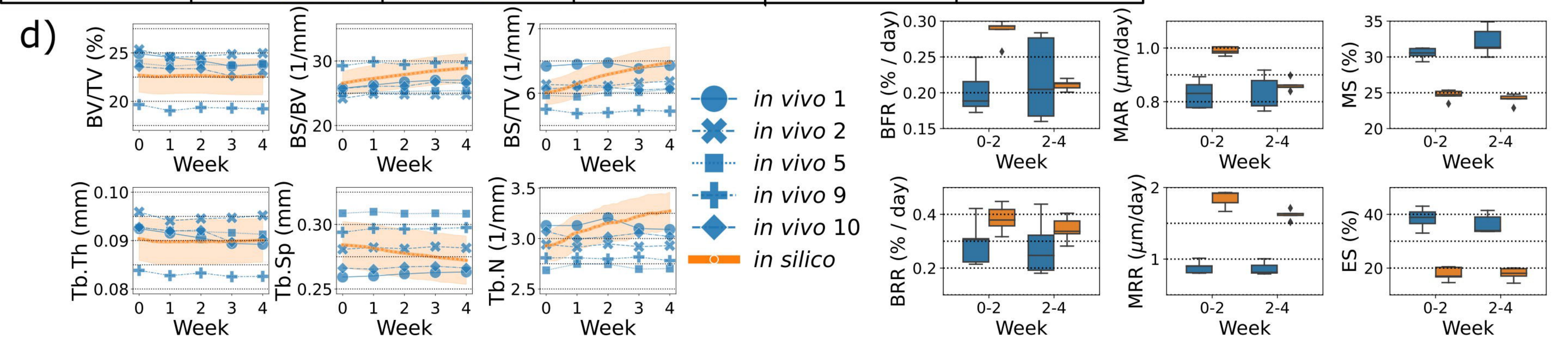
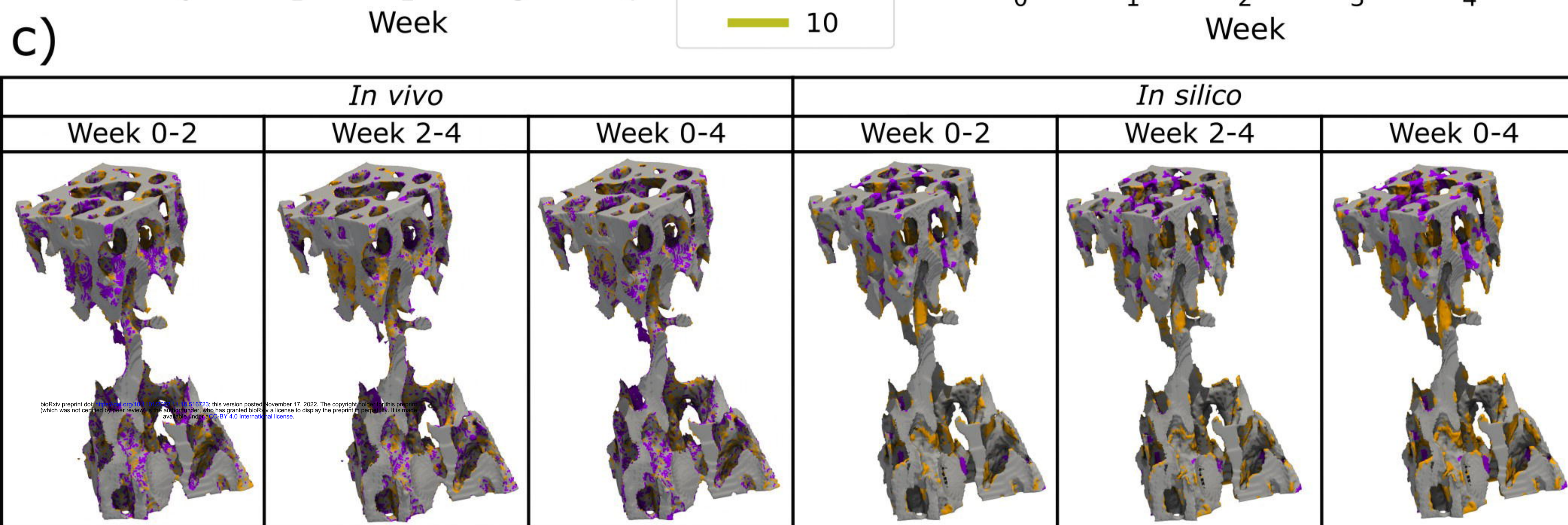
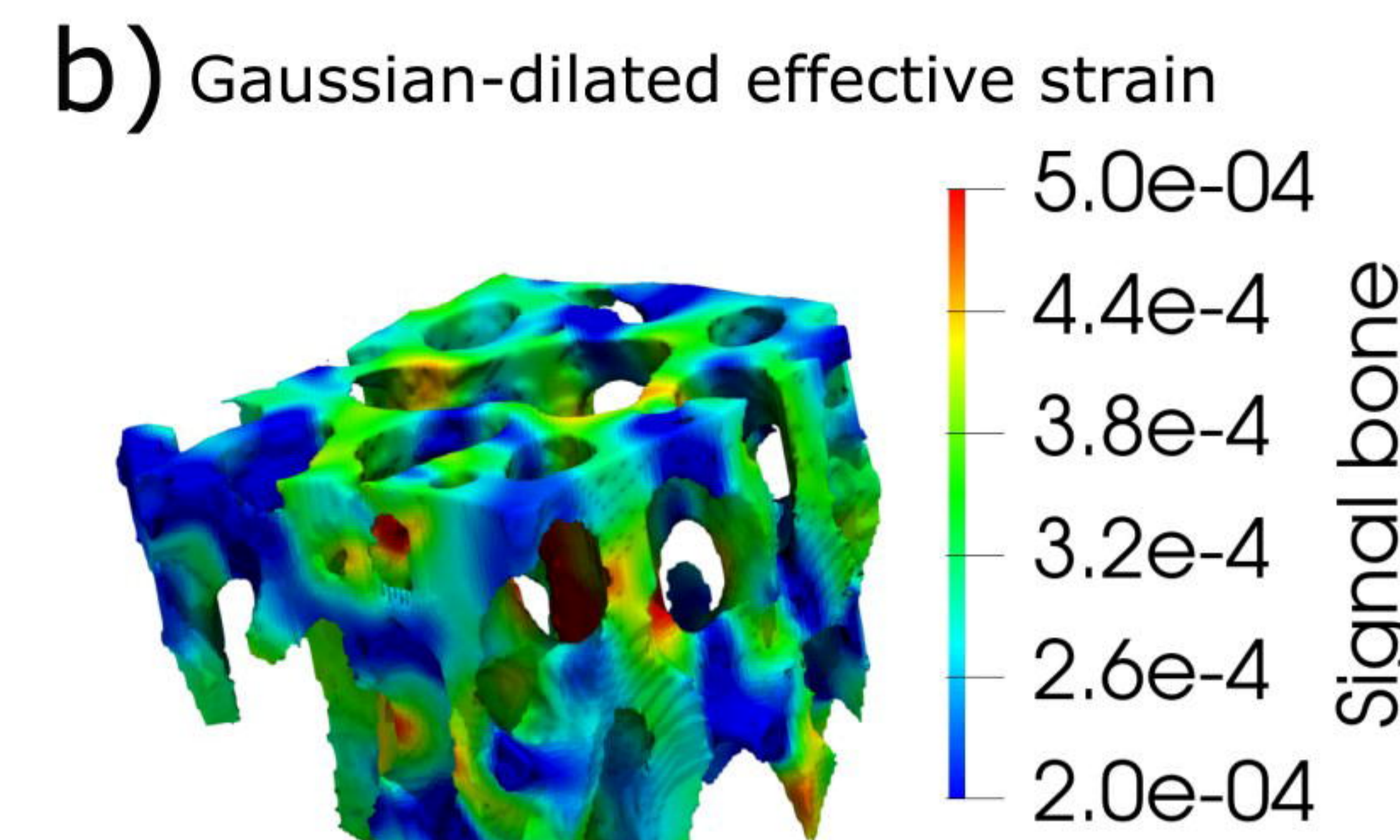
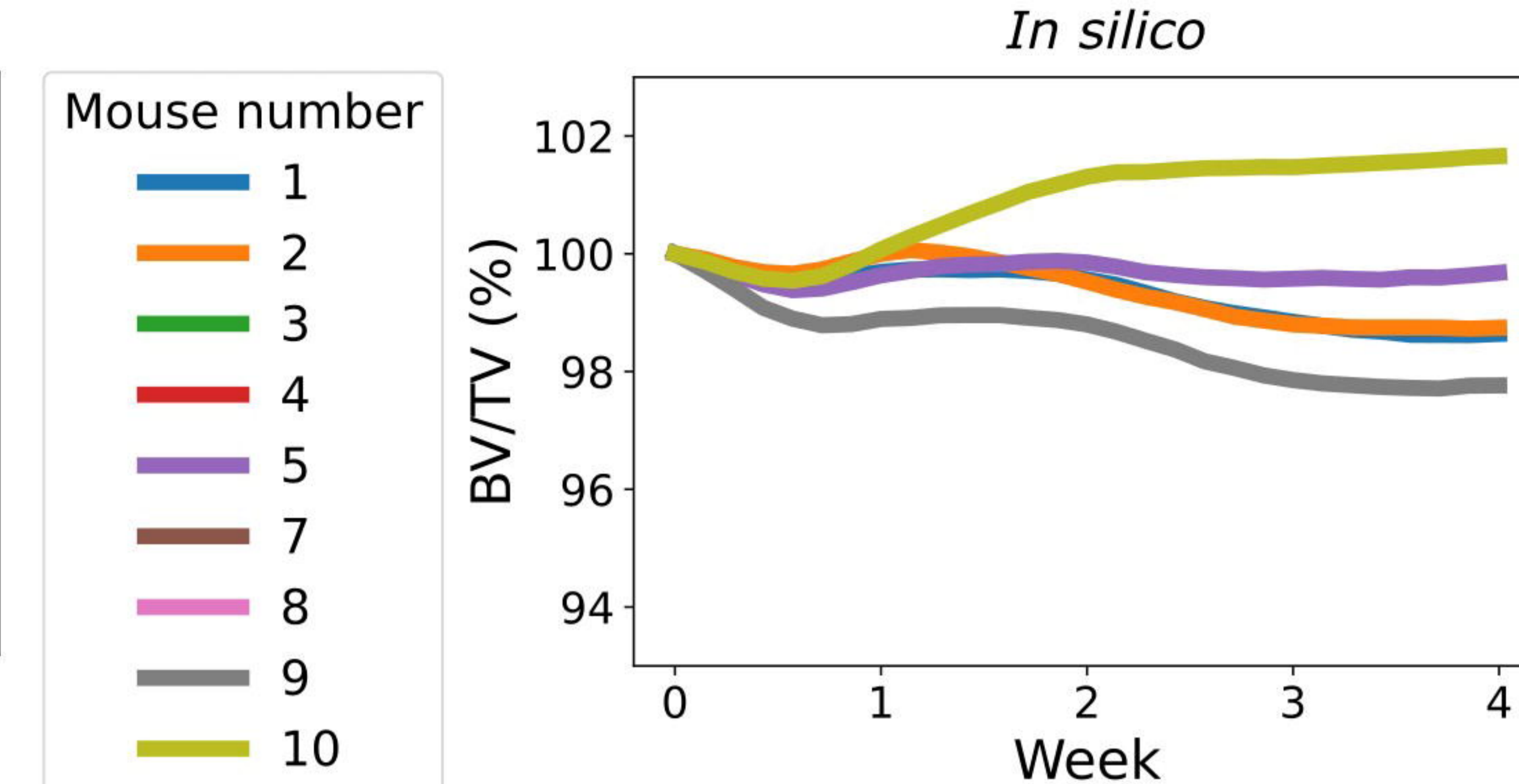
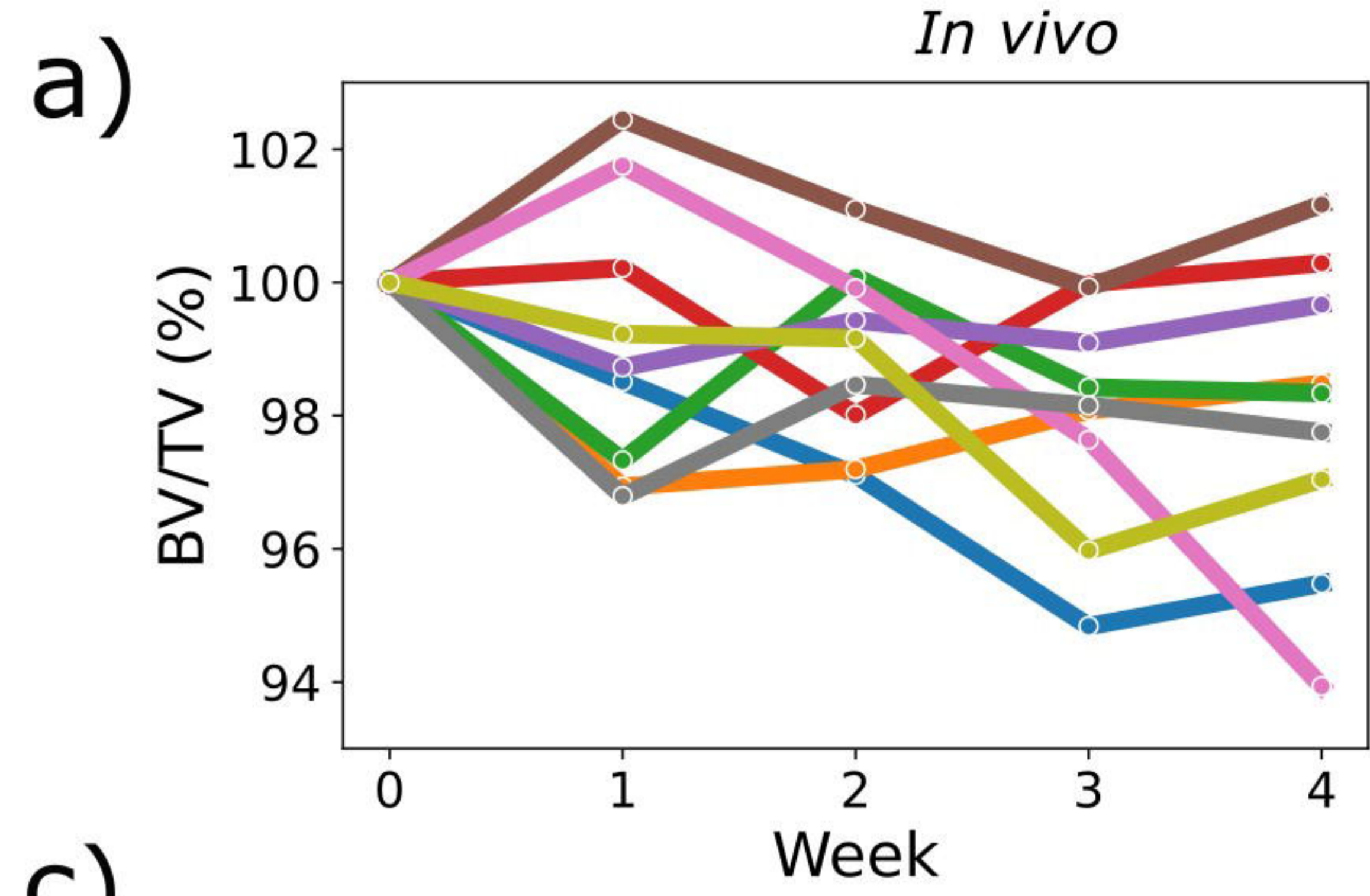




e)

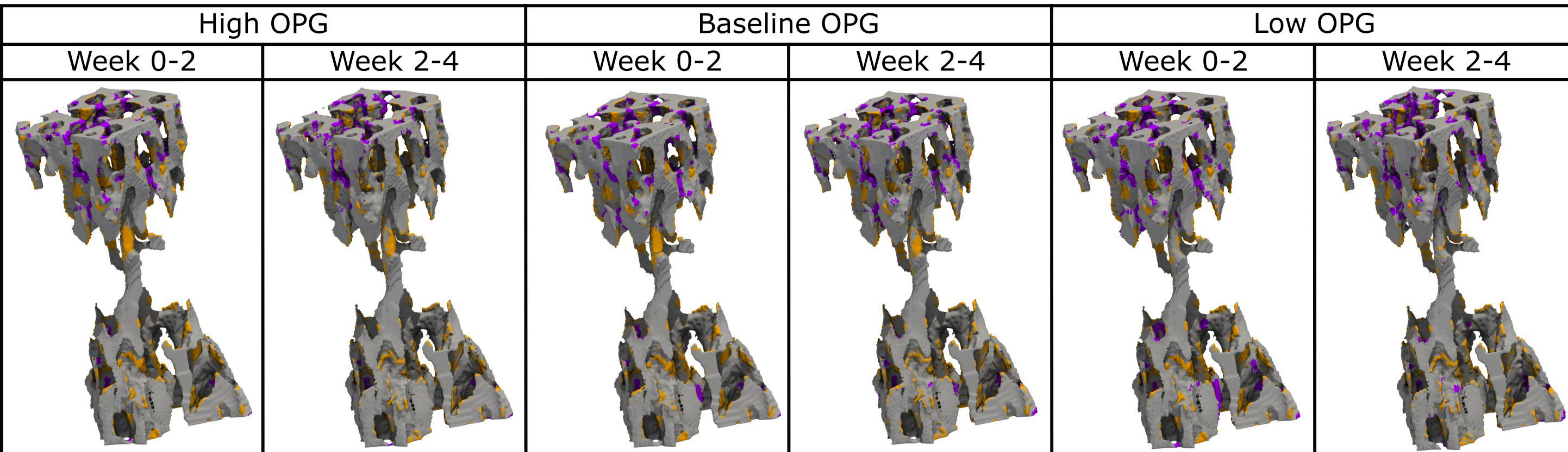




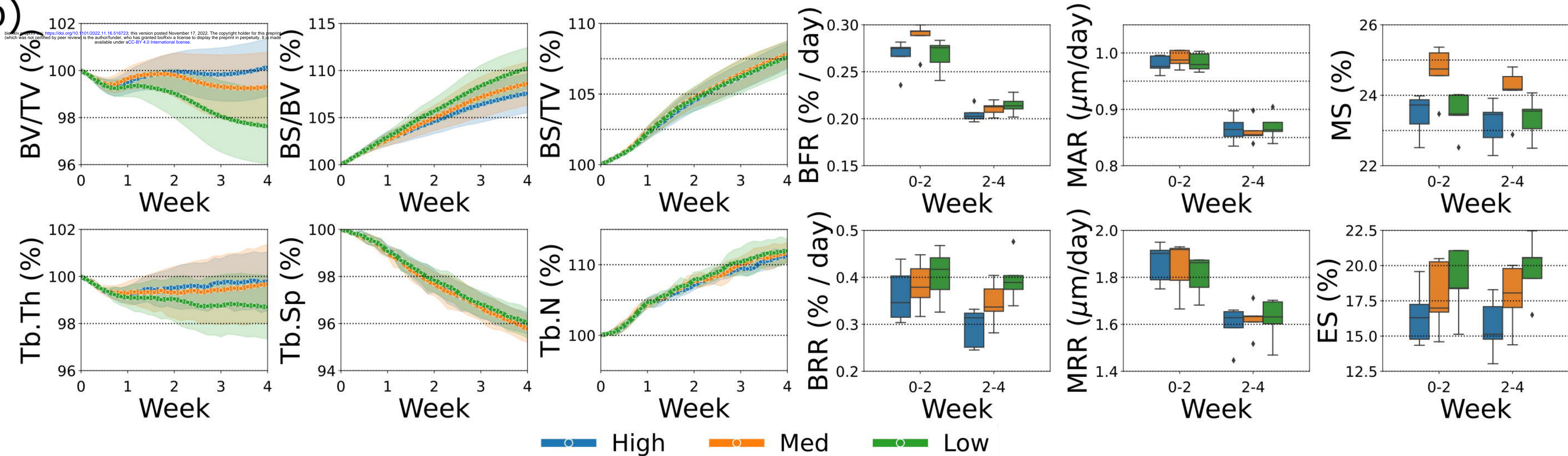




a)

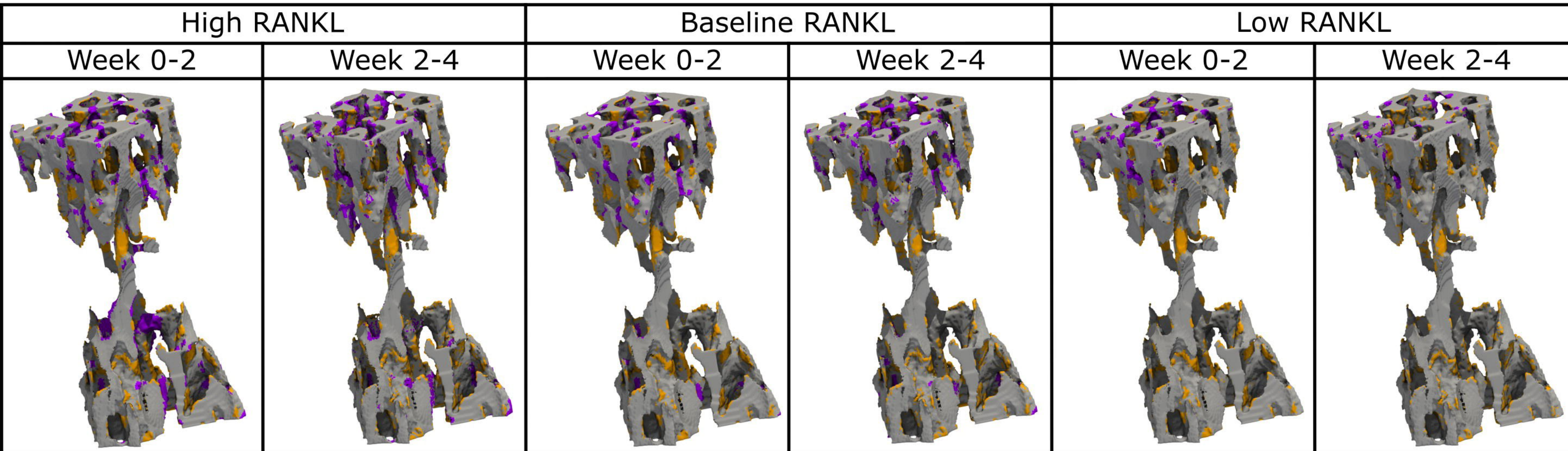


b)

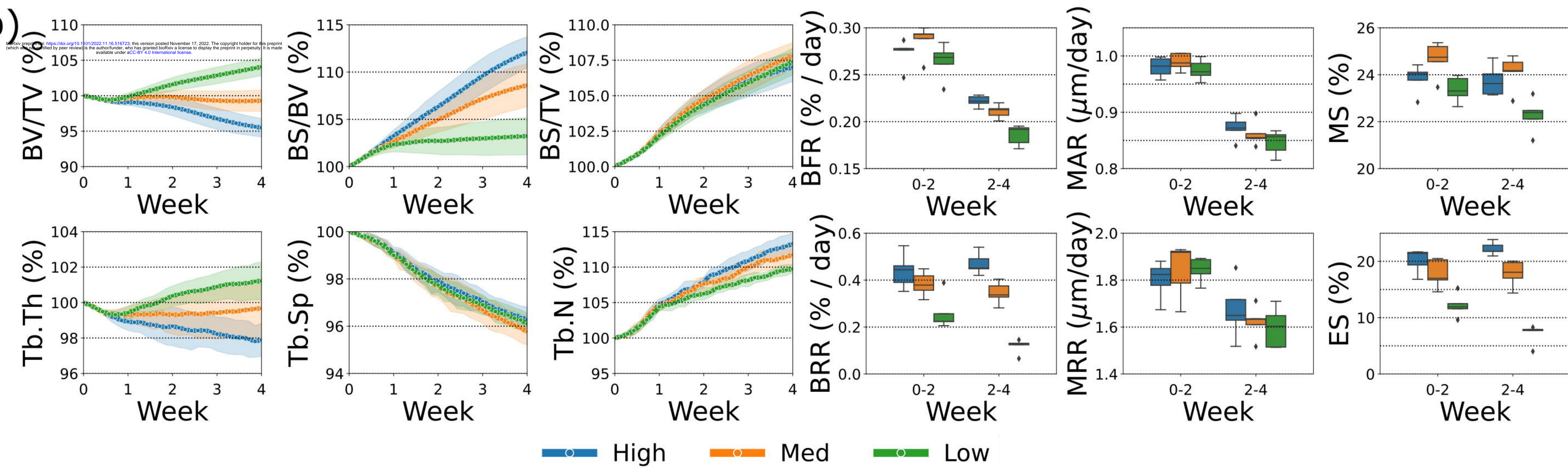




a)

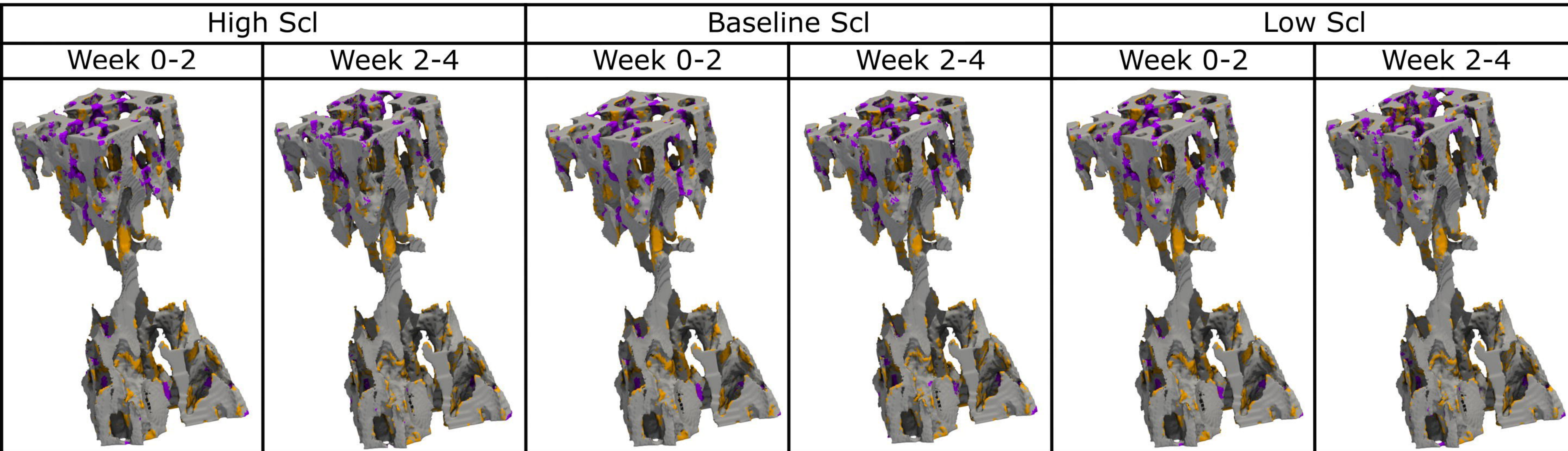


b)





a)



b)

